Dielectric Engineering Boosts the Efficiency of

Carbon Nanotube Photodiodes

Mitchell J. Senger, † Ali Kefayati, § Andrea Bertoni, ‡ Vasili Perebeinos, § Ethan D. Minot †, *

ABSTRACT

Carbon nanotube (CNT) photodiodes are a promising system for high-efficiency photocurrent generation due to the strong Coulomb interactions that can drive carrier multiplication. If the Coulomb interactions are too strong, however, exciton formation can hamper photocurrent generation. Here, we explore, experimentally and theoretically, the effect of the environmental dielectric constant (ε_{env}) on the photocurrent generation process in CNTs. We study individual ultra-clean CNTs of known chiral index in vacuum or dry nitrogen gas ($\varepsilon_{env} = 1$) and oil ($\varepsilon_{env} = 2.15$). The efficiency of photocurrent generation improves by more than an order of magnitude in oil. Two mechanisms explain this improvement. First, the refractive index of the environment optimizes the interference between incident and reflected light. Second, exciton binding energies are reduced in oil, changing the relaxation pathways of photoexcited carriers. We varied the axial electric field in the pn junction from 4 to 14 V/ μ m. Our measurements at high field indicate that autoionization of second-subband excitons can coexist with carrier multiplication. Dielectric screening makes this coexistence regime more accessible and allows us to reach photocurrent quantum yields greater than 100%.

[†]Department of Physics, Oregon State University, Corvallis, Oregon 97331, United States,

[§]Department of Electrical Engineering, University at Buffalo, The State University of New York, Buffalo, NY 14260, United States,

[‡]Istituto Nanoscienze-CNR, Via Campi 213a, I-41125 Modena, Italy

KEYWORDS

carbon nanotube, photodiode, dielectric engineering, quantum efficiency, exciton dissociation, graphene

TEXT

A hallmark of low-dimensional materials, such as carbon nanotubes (CNTs), is the strong Coulomb interaction between charge carriers. Experiments with CNT photodiodes have shown that strong Coulomb interactions can lead to carrier multiplication and, potentially, high-efficiency photocurrent generation. While these results are encouraging, Coulomb interactions can also be problematic for photocurrent generation. When the attraction between electrons and holes is too strong, photocurrent generation is hampered by exciton formation. Therefore, in applications such as solar energy harvesting and optical sensing, a balance must be found between the beneficial/detrimental effects of Coulomb interactions.

The Coulomb interaction energy scale in CNTs is $E_C = e^2/4\pi\varepsilon_0\varepsilon_{\rm eff}D$ where D is the CNT diameter, e is the electron charge, ε_0 is vacuum permittivity, and $\varepsilon_{\rm eff}$ is the effective relative dielectric constant for charge-charge interactions. This interaction energy can be tuned by both $\varepsilon_{\rm eff}$ and D. Diameter tuning was the focus of a previous experiment on CNT photodiodes.⁴ The importance of dielectric environment, however, has not been experimentally tested for the CNT photodiode system.

Previous authors have explored the effect of dielectric environment on exciton resonances in CNTs. Early experiments utilized dielectric liquids,^{6–8} and more recent work included molecular coatings, and boron nitride coatings, to tune the dielectric environment around a CNT.^{9–12} There have been parallel efforts to study the role of dielectric environment in other low-dimensional optoelectronic materials such as single-layer transition metal dichalcogenides.^{13–16} None of these dielectric engineering experiments have included measurements of photocurrent quantum yield.

In this work, we explore the effect of the dielectric environment on the photocurrent generation process in CNTs. We fabricated CNT photodiodes from individual ultra-clean suspended CNTs. The photocurrent was characterized in vacuum or dry nitrogen gas (an environment with relative

environmental dielectric constant $\varepsilon_{\rm env}=1$), and then in dielectric oil ($\varepsilon_{\rm env}=2.15$). Upon changing to the oil environment, we observed large increases in photocurrent. Our modeling of the system shows that the increased photocurrent is due to changes in photocurrent quantum yield, η , as well as changes in the optical cavity formed by the CNT and the underlying reflective surface. Our experiments cover a wide range of axial electric field (up to 14 V/ μ m), allowing us to determine the electric field threshold for $\eta > 100$ %.

RESULTS AND DISCUSSION

Figure 1a shows an electron microscope image of a suspended CNT device. To ensure an ultraclean CNT, the CNT growth process is the last step in the fabrication process (see Methods). We pre-screen devices to find those with a single semiconducting CNT connecting the electrodes. The pre-screening experiments include transistor characteristics (the transistor must have a sharp on/off threshold), scanning photocurrent microscopy (photocurrent must come from a single location), and photocurrent spectroscopy (exciton resonances must be associated with a single chiral index). The CNT devices that pass these tests are wire-bonded and placed in an optical cryostat (Janis). The chiral indices of the CNT are determined by measuring the exciton resonance energies and comparing these energies to atlas data.¹⁷

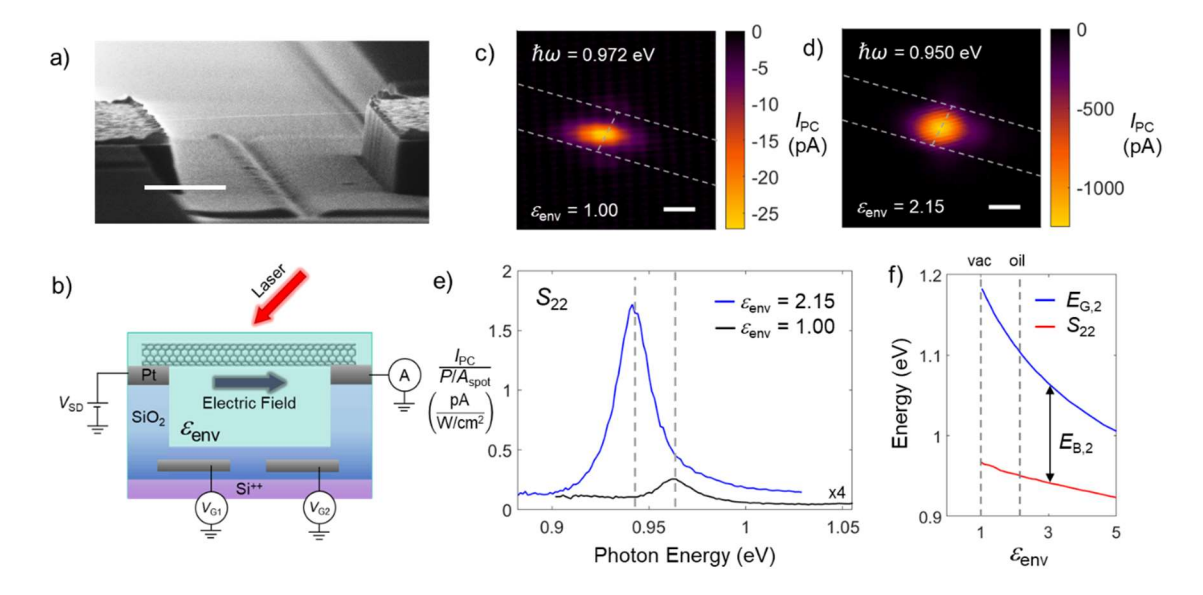


Figure 1. a) An SEM image of a suspended CNT device. Scale bar is 1 μm. b) Electrical schematic of the device. Split gate voltages ($V_{\rm G1}$, $V_{\rm G2}$) can be independently tuned. A bias voltage ($V_{\rm SD}$) is applied between the source and drain electrodes and current is measured using a preamplifier (Stanford Research). The dielectric environment is either vacuum, dry nitrogen, or dielectric oil. c) Scanning photocurrent microscope image of Device 1 in dry nitrogen with $V_{\rm G1} = -V_{\rm G2} = 5$ V, and $V_{\rm SD} = -0.5$ V. The edges of the source and drain electrodes are shown with dashed lines. Scale bar is 2 μm. d) Scanning photocurrent microscope image of the device in dielectric oil with $V_{\rm G1} = -V_{\rm G2} = 4$ V, and $V_{\rm SD} = -0.5$ V. Scale bar is 2 μm. e) Photocurrent spectra near the $S_{\rm 22}$ resonance, measured in dry nitrogen and oil environments. The photon energy is scanned using a double monochromator that transmits a 5 meV bandwidth. $V_{\rm G1} = -V_{\rm G2} = 8$ V and $V_{\rm SD} = -0.5$ V. f) Calculated values for the bandgap of the second subband, $E_{\rm G2}$, the exciton resonance of the second subband, $S_{\rm 22}$, and the exciton binding energy of the second subband, $E_{\rm B,2}$. The calculation assumes a (22,6) CNT.

All measurements were performed at room temperature with the CNT first in vacuum (or dry nitrogen gas) and then in dielectric oil. We chose an oil that is designed for vacuum pumps (HyVac) because it is an excellent insulator (no measurable conductance). The dielectric response of the oil was measured with an Abbe refractometer (see S.I.). The diode characteristics were checked in both environments by applying gate voltages $V_{G1} = 5$ V and $V_{G2} = -5$ V. For all devices reported here, we observed rectifying behavior ($I_{SD} < 1$ pA for reverse bias up to -2 V) and an exponentially increasing current in forward bias with ideality factor ~ 1.2 (see Section 1 of the S.I.).

Figure 1 shows photocurrent images and spectra from the same CNT (Device 1) in dry nitrogen gas ($\varepsilon_{\rm env} = 1$) and in oil ($\varepsilon_{\rm env} = 2.15$). The photocurrent measurements were performed with a small bias ($V_{\rm SD} = -0.5 \text{ V}$) which increases the length of the intrinsic region and therefore boosts the photocurrent signal (see Section 4 of the S.I.). ¹⁹ The CNT's chirality was determined with broadband photocurrent spectra to be (22, 6), corresponding to diameter D = 2.0 nm and chiral angle $\theta = 11.7^{\circ}$. Scanning photocurrent microscopy images were taken with the light-source tuned to $\hbar\omega = S_{22}$. The shape of the peak in the photocurrent images (Fig. 1c & d) corresponds to the shape of the laser spot. 19 Photocurrent originates from the intrinsic region of the diode which is smaller than the point spread function of the laser. In the oil environment, the point spread function is modified slightly because the thin layer of oil interacts with the laser path. The two photocurrent spectra in Figure 1e were taken in different environments, with all other parameters were the same ($V_{\rm G1} = -V_{\rm G2} = 8 \text{ V}$ and $V_{\rm SD} = -0.5 \text{ V}$). The current is normalized by the laser power, P, and the area of the beam spot, $A_{\text{spot}} = P/I_{\text{max}}$, where I_{max} is intensity at the center of the spot). For all spectral measurements $I_{\text{max}} < 30 \text{ W/cm}^2$, which ensured a linear relationship between laser intensity and photocurrent.⁴ When the CNT was introduced to the oil environment, the S_{22} exciton resonance was redshifted by 21 meV, and the normalized photocurrent peak increased by 27-fold. This boost in photocurrent, which was observed upon increasing $\varepsilon_{\rm env}$, is the central focus of this paper.

We first verified that the 21-meV redshift is consistent with the theory. Ando calculated the transition energies of the first and second subbands of semiconducting CNTs surrounded by a dielectric material. In general, the CNT bandgap, the exciton binding energy, and the exciton resonance energy are all expected to diminish as ε_{env} is increased. In Fig. 1f, we plot the predicted values for S_{22} and the band gap of the second subband, $E_{G,2}$, as a function of ε_{env} for a CNT with chiral index (22, 6). For this specific chiral index, Ando's theory predicts a 17 meV redshift in S_{22} when ε_{env} is changed from 1 to 2.15, in good agreement with our measured photocurrent spectra. Our analysis of the red shift could be refined further if we identified the presence/absence of molecular adsorbates on the CNT surface prior to submersion in oil. Nonetheless, the 21-meV redshift (Fig. 1e) is convincing evidence that submersion in oil caused a significant increase in ε_{env} .

One of the mechanisms controlling the photocurrent magnitude (Fig. 1e) is optical interference. Light is reflected from the gate electrodes and a standing wave pattern is established above the gate electrodes. The optical field intensity at the position of CNT *pn* junction is sensitive to the incident wavelength, the refractive index of the environment, and the height of the CNT above the gates. We have characterized these optical interference effects using finite difference time domain (FDTD) simulations with Lumerical FDTD (see S.I.).²⁰

To verify our FDTD simulations of optical interference, we performed a control experiment using suspended graphene on top of the electrode structure (the CNT was replaced with a graphene sheet, Fig. 2a). Graphene is optically transparent (97.7% transparency for visible wavelengths²¹) and is used here as an ultra-thin light source at the position of interest. We generated incandescence from the suspended graphene by Joule heating in a vacuum environment (Fig. 2b).²² In vacuum, there is no path for thermal conduction out of the graphene plane and the graphene reaches temperatures above 1000 K with a source-drain bias of ~ 4 V. Figure 2c shows the resulting emission spectrum collected through a microscope objective and a fiber optic spectrometer (see the S.I. for experimental details). There is a dip in the spectrum at a wavelength of ~ 700 nm (Fig. 2c) corresponding to destructive interference between the direct and reflected optical paths (the direct path interferes destructively with light that is reflected from the gate electrodes). The measured spectrum agrees well with our FDTD simulations. The red dashed line in Fig. 2c was calculated by using a blackbody emission temperature of 1400 K (Fig. 2d), the response function of the spectrometer (Fig. 2e), and the interference contrast calculated by FDTD (Fig. 2f). We conclude that the FDTD calculations are a reliable tool for modeling optical interference caused by our electrode structure.

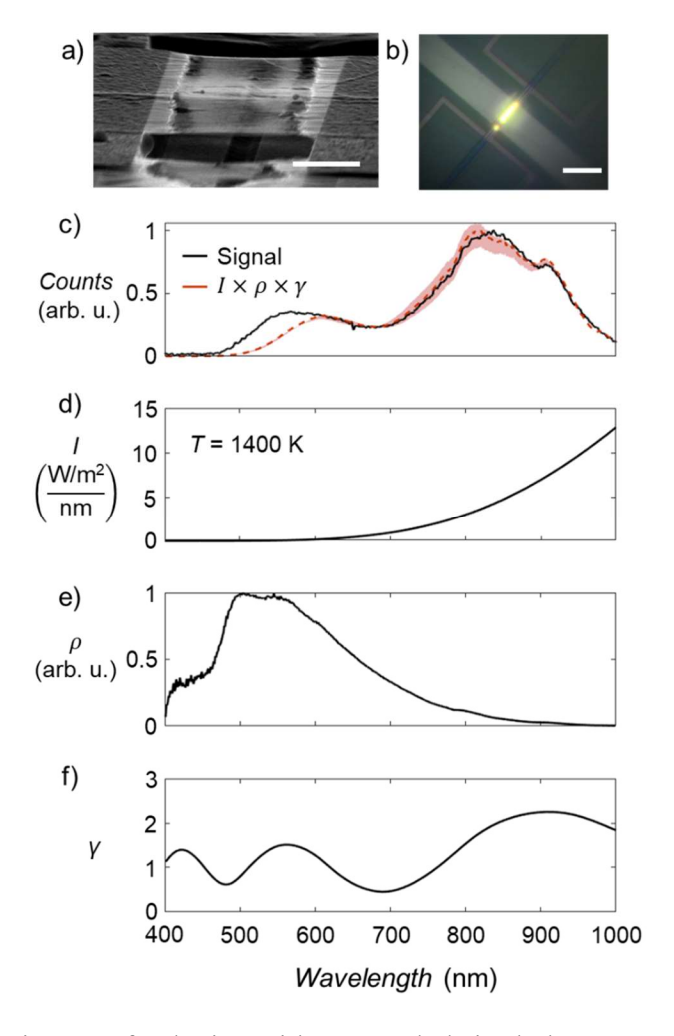


Figure 2. a) An SEM image of a device with suspended single layer graphene substituted for a CNT. Scale bar is 1 μ m. b) Optical micrograph of the same device while the graphene is incandescing. Scale bar is 20 μ m. c) Black line: Incandescence spectrum of graphene as measured by the spectrometer. Spectrum is smoothed with a moving average with 3 nm spectral width. The red dashed line shows a simulated emission spectrum based on FDTD calculations of interference effects. The red shaded area shows the simulation result when the incandescent source is moved up or down by 10 nm. d) Simulated blackbody luminosity spectrum with T = 1400 K. e) Responsivity of the spectrometer that was used to measure the incandescence spectrum of the graphene sheet. f) FDTD calculation of optical interference when the graphene is 650 nm above the gate electrodes.

After establishing the intensity of the optical field, we now proceed to analyze the photocurrent spectrum as a function of the axial electric field. Figures 3a and b show the photocurrent spectra associated with the S_{22} exciton resonance while varying the gate voltages $V_G = V_{G1} = -V_{G2}$. The

 S_{22} resonance peak shifts towards lower energy as the gate voltages are increased. The S_{33} resonance peak (not shown in Fig. 3) shifts toward higher energy as the gate voltages are increased (see Section 9 of the S.I.). At the largest gate voltages in oil ($V_G = 33 \text{ V}$) the shifts in S_{22} and S_{33} peak position are $\Delta E_{22} = -50 \text{ meV}$ and $\Delta E_{33} = +21 \text{ meV}$.

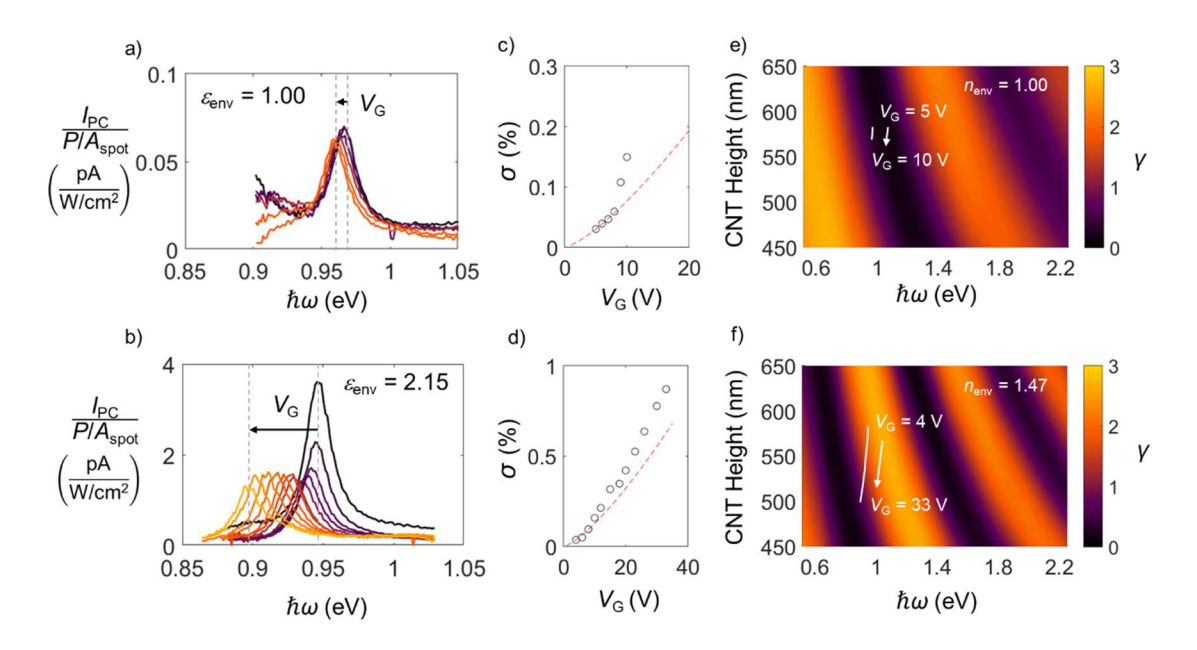


Figure 3. a) Photocurrent spectra normalized for laser intensity in the vicinity of S_{22} in vacuum with $V_{\rm SD} = -0.5$ V. The peak shifts by 7 meV as $V_{\rm G}$ is increase from 5 to 10 V. b) Photocurrent spectra normalized for laser intensity in the vicinity of S_{22} in dielectric oil with $V_{\rm SD} = -0.5$ V. The peak shifts by -50 meV as $V_{\rm G}$ is increased from 4 to 33 V. c) Black circles show the mechanical strain, σ , calculated from the peak shift of the S_{22} resonance in vacuum. The red dashed line shows the strain calculated by the electromechanical model when $\varepsilon_{\rm env} = 1$. (see S.I.). d) Black circles show the mechanical strain, σ , calculated from the energy of the peak shift of the S_{22} resonance in dielectric oil. The red dashed line shows the strain calculated by the electromechanical model when $\varepsilon_{\rm env} = 2.15$. e) FDTD calculation of γ when $n_{\rm env} = 1$. The white line shows the CNT's height, and the S_{22} resonance energy, as $V_{\rm G}$ is increased. f) FDTD calculation of γ when $n_{\rm env} = 1.47$. The white line shows the CNT's height, and the S_{22} resonance energy, as $V_{\rm G}$ is increased.

We attribute the peak shift (Fig. 3a and b) to a combination of two mechanisms: (i) the gate voltages generate an electric field along the axis of the CNT, thereby changing the exciton binding energy, (ii) electrostatic forces between the CNT and the gate electrodes cause mechanical strain in the CNT, thereby modifying the CNT band structure. The first mechanism

(the Stark effect) has been estimated theoretically for CNTs.²³ For an axial electric field of ~ 10 V/µm, all exciton resonances are predicted to red shift by approximately 10 meV. The second mechanism (strain-induced changes in band structure) was studied in detail by Huang *et al.*²⁴ The strain is $\sigma = \Delta L/L_0$ where L_0 is the original length of the suspended CNT and ΔL is the change length. For the (22, 6) chiral index, the strain-induced shift in exciton resonance is expected to be 45 meV per percent strain. The S_{22} resonance is expected to red shift with strain, while the S_{33} resonance is expected to blue shift by an equal magnitude. Based on these peak-shifting mechanisms, we understand the change in peak position as follows. At the maximum gate voltage in oil, the S_{22} resonance has a Stark shift of -14 meV and a strain-induced shift of -36 meV (corresponding to $\sigma = 0.8\%$), yielding a total shift of -50 meV. Similarly, the S_{33} resonance has a Stark shift of -14 meV and a strain-induced shift of +36 meV, yielding a total shift of +22 meV. Figure 3c and d (black circles) shows σ calculated from the S_{22} and S_{33} peak positions at various gate voltages (see S.I. for details).

To confirm the strain values (Fig. 3c and d) we constructed an electromechanical model of the system. We solved for the bended geometry of the CNT resulting from the competition between the electrostatic pulling force and CNT stretching stiffness (see S.I). 25 The electromechanical model accounts for the charge density on the CNT, the mechanical elasticity of the CNT, and ε_{env} . As the gate voltages are increased, the CNT bends and stretches along its axis in response to the electrostatic force from the gates (Fig. S19). Results from the electromechanical model are plotted in Fig. 3c and d (red dashed line). There are no free parameters in the electromechanical model. The model is in good agreement with the experimental result (black circles).

Figure 3e and f summarize our FDTD calculations of the optical intensity at the location of the CNT pn junction. The optical intensity is modulated due to optical interference between the incident and reflected light (standing wave pattern). We define the intensity enhancement factor, γ , relative to a fictional device that has no reflective surface under the CNT. γ depends on the height of CNT above the reflective gates, and the photon wavelength. For the oil environment, we see more nodes in γ due to the greater refractive index of the environment ($n_{\text{env}} = \sqrt{\varepsilon_{\text{env}}} = 1.47$ at $\hbar\omega = 0.95$ eV).

The FDTD calculations (Fig. 3e and f) highlight the importance of knowing the initial height of the CNT, and any changes in height during an experiment. The white lines on Fig. 3e and f show the calculated heights from our model of the electrostatic forces pulling the CNT towards the gates. In the oil environment, the model predicts that the center point of the CNT drops in height by 90 nm as V_G is increased from 4 to 33 V. This change in height has a significant effect on γ , causing γ to drop from 2.29 to 0.57.

Figures 3e and f explain some of the boost in photocurrent when the device was submerged oil. In the vacuum environment, at $V_G = 8$ V, the S_{22} resonant photon energy corresponds to $\gamma = 0.25$. In the oil environment, at $V_G = 8$ V, the S_{22} resonant photon energy corresponds to $\gamma = 2.05$. This 8-fold increase in γ partially explains the observed 27-fold increase in photocurrent (Fig. 1e). However, to understand the full effect of dielectric engineering, we now turn to analyzing the photocurrent quantum yield in the different dielectric environments.

Using the data in Fig. 3, we can estimate the photocurrent quantum yield in both vacuum and oil environments. The photocurrent produced by photons of energy $\hbar\omega$ can be calculated as $I_{PC}(\hbar\omega) = e\eta\Phi LN_L\alpha(\hbar\omega) \tag{1}$

where e is the elementary electric charge, $\Phi = P\gamma/(A_{\rm spot}\hbar\omega)$ is the photon flux, $\alpha(\hbar\omega)$ is the spectral absorption cross-section per carbon atom, $N_{\rm L}$ is the number of carbon atoms per length of the CNT (see S.I.), and L is the length of the intrinsic region in the CNT pn junction. The length of the intrinsic region is a critical parameter in this calculation. When photons are absorbed in strongly doped p-type and n-type segments of CNT (outside the intrinsic region), the photoexcited carriers quickly recombine via Auger processes. Photocurrent is only generated by photons that are absorbed in the intrinsic region.

To find the length of the intrinsic region, L, we used a self-consistent electrostatics simulation. The same method was used previously by McCulley $et\ al.^4$ The detailed calculation is presented in the S.I. A useful and instructive approximation for L can be obtained as follows. First, a two-dimensional electrostatics simulation was used to find the electric fields generated by the electrode structure. The boundary conditions of the simulation were defined by the electrode voltages and a 2D Poisson solver was used to find potential as a function of position. At a

position 650 nm above the gate electrodes, and half-way between the source-drain electrodes, we find a horizontal electric field $F_{\text{ext}} = 1.73 \times V_{\text{G}} / L_0$, where $L_0 = 2.6 \, \mu \text{m}$. To find L, we assume that the voltage drop across the pn junction, $V_{\text{SD}} - E_{\text{G}}/e$, is equal to the product LF_{ext} . This approximation is excellent when $L > 200 \, \text{nm}$ (see the dashed line in the inset of Fig. 4a). At shorter L, the electric field generated by charge on the CNT becomes increasingly important and the self-consistent calculation is necessary. The self-consistent calculation of L is plotted against V_{G} in the inset of Fig. 4a (solid line). The self-consistent calculation is also used to find F, the axial electric field at the center of the pn junction (F is slightly smaller than F_{ext}).

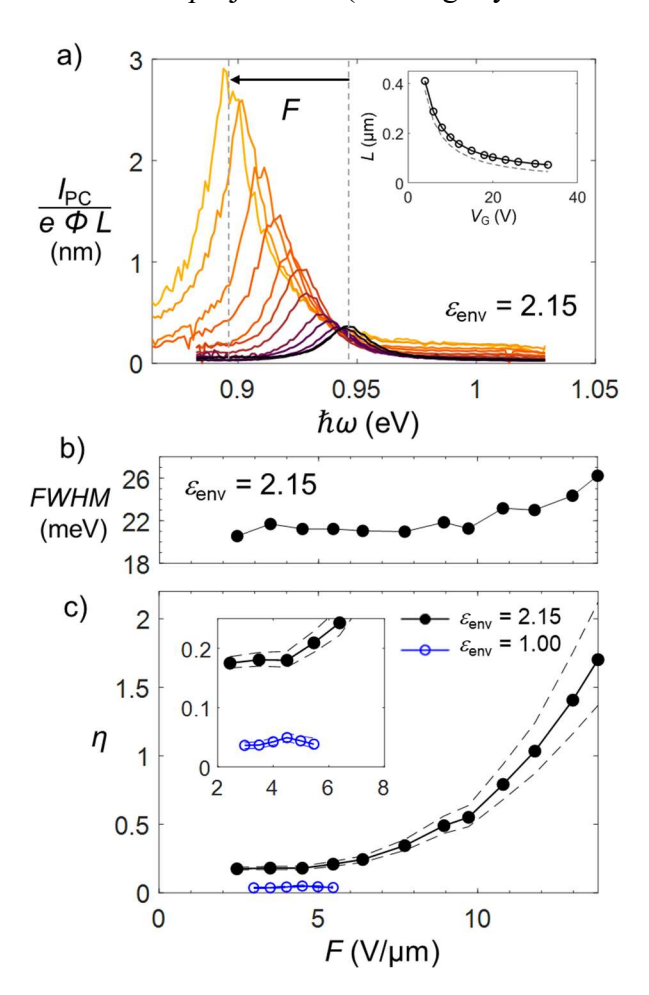


Figure 4. a) Photocurrent spectra of the S_{22} resonance normalized for the photon flux and the intrinsic region length in dielectric oil. V_G is increased from 4 to 33 V (from black curve to orange curve). The peak magnitude increases sharply with increased field. Inset: Intrinsic region length calculated self consistently (solid line) and from $F_{\rm ext}$ (dashed line). b) The full-width at half-maximum of the photocurrent peak plotted as a function of axial electric field, F. c) Calculated photocurrent quantum yield *versus* axial electric field in oil and in vacuum for

 S_{22} . Dashed lines are η_{22} calculated with the CNT's resting height increased or decreased by 10 nm.

Figure 4a shows photocurrent data from Fig. 3b that has been normalized by the factor $e\Phi L$. The photon flux, Φ , was calculated for each gate voltage using the incident light intensity and γ . After normalizing the data in this way the spectral peaks are symmetric (Lorentzian peak shape) and the maxima increase steadily with the axial electric field.

The final step to determine photocurrent quantum yield is the integration of the spectral peak $\int I_{PC} d(\hbar\omega)$. We expect the photocurrent integral to be proportional to $\int \alpha d(\hbar\omega)$, which is independent of peak broadening. Integrating both sides of Eq. 1 and solving for η_{22} we find

$$\eta_{22} = \left(\int_{S_{22}} \frac{I_{PC}(\hbar\omega)}{eL\Phi(\hbar\omega)} d(\hbar\omega) \right) / \left(\int_{S_{22}} \alpha(\hbar\omega) d(\hbar\omega) \right)$$
 (2)

The value of $\int \alpha \, d(\hbar \omega)$ is a function of the CNT chiral index.²⁸ For the chiral index of the CNT under study (22, 6), we expect $\int \alpha \, d(\hbar \omega) = 2.42 \cdot 10^{-18} \, \text{eV} \cdot \text{cm}^2$ for the S_{22} resonance.²⁸ Equation 2 yields η_{22} values for each photocurrent spectrum in Fig. 4a, allowing us to track η_{22} as a function of the axial electric field. These values are summarized in Fig. 4c for both the vacuum and oil environments. At moderate field strength, 3 to 6 V/ μ m, η_{22} is approximately 4 times larger in oil than in vacuum. In the oil environment, we tested the device at larger F and found $\eta_{22} > 1$ when $F > 11.5 \, \text{V/}\mu\text{m}$. We repeated these experiments on two additional CNT devices with D = 2.03 nm (Device 2) and D = 1.74 nm (Device 3) (see S.I.). These additional experiments were performed at the S_{33} exciton resonance. All three devices show the same key features: (1) η was larger in oil than in vacuum and (2) $\eta > 1$ in the oil environment when $F \sim 10 \, \text{V/}\mu\text{m}$. We also confirmed that $\eta_{33} > \eta_{22}$ for devices in CNTs with a similar diameter (Device 1 and Device 2 both have $D \approx 2 \, \text{nm}$).

When the CNT was submerged in oil, we observed a 4-fold increase in η_{22} when F = 3 - 6 V/µm. Theory by Ando (Fig. 1f) predicts that the oil environment weakens the S_{22} exciton binding energy from 217 meV to 155 meV (and the binding energies of other exciton species are similarly reduced). With the reduction in binding energies, we expect a greater fraction of S_{22}

excitons to decay into free carriers, rather than S_{11} , S_{12} or S_{21} excitons. Thus, our measurements are consistent with the prediction that dielectric screening promotes photocurrent generating pathways.

In the oil environment, η_{22} grows with F at fields above 5 V/ μ m. Before developing a detailed model for this behavior, we compared the measured $\eta_{22}(F)$ curve to a simple model based on carrier escape time (see S.I.). This carrier-escape-time model assumes that light is converted to free carriers which either recombine (not contributing to photocurrent) or escape from the intrinsic region (contributing to photocurrent). In this model, η grows with F because the intrinsic region shrinks at high field and the accelerating force on the carriers is greater. The model predicts a sub-linear relationship between η_{22} and F, in contrast to the super-linear $\eta_{22}(F)$ curve that we measured (Fig. 4c). We conclude that a more detailed microscopic picture is needed to explain the measured $\eta_{22}(F)$ curve.

Several processes are likely contributing to the shape of the $\eta_{22}(F)$ curve (Fig. 4c). First, the decay of S_{22} excitons generates a variety of products, some of which are weakly bound electronhole pairs.⁴ When F increases, more of these weakly bound electronhole pairs are swept out of the intrinsic region.^{2,4} Second, the branching ratios for S_{22} decay products are affected by F. As F increases, we expect a growing fraction of S_{22} excitons to decay directly into free electronhole pairs (we denote free electronhole pairs in the first and second subbands as E_{11} and E_{22} respectively). The broadening of the photocurrent peak (Fig. 4a & b) suggests that field-induced dissociation of S_{22} excitons begins contributing to the total decay rate at high field ($S_{22} \rightarrow E_{22}$). The full-width at half maximum of the photocurrent peak is initially 20 meV (consistent with the phonon-mediated relaxation pathway²⁹) and grows to 26 meV at high field. To verify this interpretation of the peak broadening, we solved the Bethe-Salpeter equation at a large field with a modified dielectric environment (see S.I.). Third, at high field, the S_{11} excitons can also be dissociated by the field. To estimate the threshold for field-induced dissociation of S_{11} excitons, we use a simplified model for the S_{11} dissociation time²³

$$\tau_{\rm diss} = \frac{\hbar F}{4E_{\rm B,1}F_0} \exp\left(\frac{F_0}{F}\right) \tag{3}$$

where F_0 is a characteristic field that depends on $E_{\rm B,1}$ and the exciton's reduced mass.²³ For a CNT with D=2 nm in oil, $E_{\rm B,1}\approx 125$ meV and $F_0\approx 35$ V/ μ m (significantly less than $E_{\rm B,1}$ and F_0 in vacuum).^{18,23} Thus, $\tau_{\rm diss}<10$ ps when $F\sim 3.1$ V/ μ m. We expect $\tau_{\rm diss}<10$ ps is sufficiently fast to outpace competing decay pathways of the S_{11} exciton, such as end quenching.

At F > 11.5 V/µm, our data suggests $\eta_{22} > 100\%$, indicating that photocurrent (number of electrons per unit time) is greater than the photon absorption rate (number of photons absorbed in the intrinsic region per unit time). Complete conversion of S_{22} into free carriers is not enough to explain $\eta_{22} > 100\%$. A possible mechanism for $\eta_{22} > 100\%$ is carrier multiplication via an impact ionization process. 1,5,30,31 We postulate that free carriers in the second subband (E_{22}) can undergo impact ionization at the fields used in our experiment. In bulk semiconductors, the impact ionization process would not be significant because the threshold field for impact ionization is several tens of volts per micron. 32 For CNTs, however, the threshold field is estimated to be ~ 7 times smaller than a bulk material with the same band gap given the same excitation energy. 30,31 We expect impact ionization rates to be significant when $F \sim E_G/e\ell_{op} \sim 10$ V/µm where ℓ_{op} is the optical phonon scattering length. 30

To make our analysis more quantitative, we employ master equations for the light-induced populations of excited states in the intrinsic region. To describe the generation and decay of S_{22} , E_{22} and E_{11} states we have

$$\frac{\partial n_{S_{22}}}{\partial t} = 0 = \Phi L N_{L} \alpha(\hbar \omega) - \frac{n_{S_{22}}}{\tau_{\text{tot } S_{22}}},\tag{4}$$

$$\frac{\partial n_{E_{22}}}{\partial t} = 0 = \frac{n_{S_{22}}}{\tau_{\text{diss},S_{22}}} - \frac{n_{E_{22}}}{\tau_{\text{tot},E_{22}}},\tag{5}$$

$$\frac{\partial n_{E_{11}}}{\partial t} = 0 = \frac{n_{S_{22}}}{\tau_{S_{22} \to E_{11}}} + \dots + \frac{n_{S_{11}}}{\tau_{\text{diss}, S_{11}}} + \frac{3n_{E_{22}}}{\tau_{\text{ii}, E_{22}}} + \frac{2n_{E_{12,21}}}{\tau_{\text{ii}, E_{12}}} - \frac{I_{PC}}{e},\tag{6}$$

where $1/\tau_{\text{tot},S_{22}}$ and $1/\tau_{\text{tot},E_{22}}$ are the total decay rates of S_{22} and E_{22} , respectively. $1/\tau_{\text{diss},S_{22}}$ and $1/\tau_{\text{diss},S_{11}}$ are the field-induced dissociation rates of S_{22} and S_{11} , respectively. $1/\tau_{\text{ii},E_{22}}$ and $1/\tau_{\text{ii},E_{12}}$ are the impact ionization rates of E_{22} and $E_{12,21}$, respectively. Similar equations govern the populations of S_{11} and $S_{12,21}$ and $E_{12,21}$. Equation 6 describes the generation of E_{11} states by

several pathways: the decay of S_{22} (the first term on the right-hand side); the decay of $S_{12,21}$, E_{22} , and $E_{12,21}$ (not shown explicitly); field-induced dissociation of S_{11} ; and impact ionization. We assume that all E_{11} states leave the system as photocurrent, I_{PC} . In principle, free carriers in all the bands could contribute to impact ionization if they are sufficiently accelerated by the electric field. However, free carriers in the second subband have larger initial energy and will more likely exceed the energy threshold for carrier multiplication.^{1,4}

Solving these master equations requires energy-resolved carrier densities and energy-resolved rates, which is beyond the scope of this work. However, the master equations give insight into the role of dielectric environment. The S_{22} dissociation rate is sensitive to F and $\varepsilon_{\rm env}$ (increasing $\varepsilon_{\rm env}$ reduces the exciton binding energy and boosts $1/\tau_{{\rm diss},S_{22}}$). When $1/\tau_{{\rm diss},S_{22}}$ is comparable to $1/\tau_{{\rm tot},S_{22}}$, we expect a significant occupation of E_{22} states. These free carriers in the second subband drive the impaction ionization terms in Eq. 6. When F is sufficient to dissociate S_{22} , the field is also sufficient for impact ionization.

CONCLUSIONS

We characterized the performance of CNT photodiodes in different dielectric environments. To analyze our experiments, we modeled the static electric field, band filling, optical field, and electromechanical effects in the system. The optical field was verified with interference measurements, and the electromechanical model was verified with strain measurements. We found a significant improvement in photocurrent quantum yield in the oil environment compared to the vacuum environment. To explain this result, we considered the effect of dielectric screening on the energy relaxation pathways of photoexcited carriers. When $\varepsilon_{env} = 1$, photoexcited carriers are more likely to be bound as excitons. When $\varepsilon_{env} > 1$, however, photoexcited electrons and holes are more likely to escape as free carriers and contribute to the photocurrent. We extended our experiments to a large axial electric field and found the threshold for $\eta > 100\%$. We attribute $\eta > 100\%$ to an impact ionization pathway and our calculations show that dielectric screening promotes this pathway. We conclude that dielectric engineering offers a route to optimizing the performance of photodiodes made from CNTs. These ideas can be extended to photodiodes made from other low-dimensional materials, including transition metal dichalcogenides.

METHODS

CNTs were grown in a fast chemical vapor deposition (CVD) process on a pre-patterned electrode structure. 4,19,33 The electrode structure was fabricated on a Si/SiO₂ substrate (300 nm SiO₂). First, a pair of gate electrodes (60 nm Pt) were deposited *via* e-beam evaporation. The gates were buried in 600 nm SiO₂, then, source and drain electrodes (60 nm Pt) were patterned above the gate electrodes. A trench was created between the source and drain electrodes by reactive ion etching (the electrodes act as an etch mask). The etch was stopped with 50 nm of SiO₂ covering the gates. The catalyst for CNT growth is a stack of Cr/SiO₂/Fe (2 nm/30 nm/1.5 nm) which was patterned on top of the source and drain electrodes. CVD growth is done in a 1-inch tube furnace at 800°C. The gas flow is a mixture of H₂ and Ar (0.45 SLM) which is split between two bubblers (methanol bubbler with 0.15 SLM gas flow, and ethanol bubbler with 0.3 SLM gas flow). The device sits in the hot zone of the furnace for 5 minutes. After growth, the CNT was exposed to ambient air for approximately 3 hours while the devices were electrically probed and wire bonded. Initial photocurrent measurements were made in either vacuum (Janis optical cryostat) or under a stream of dry nitrogen gas. In these two environments (denoted as $\varepsilon_{env} = 1$) photocurrent measurements were equivalent.

For all photocurrent measurements, the CNT device is illuminated with a supercontinuum laser (NKT SuperK) with 320 MHz pulse rate filtered by a double monochromator (Princeton Instruments) to a ~ 5 nm linewidth with accessible wavelengths ranging from 400 - 1800 nm. To acquire photocurrent images, the laser was focused to the plane of the CNT and rastered over the sample via a pair of computer-controlled galvo mirrors (Nutfield). As the laser is scanned over the sample, the photocurrent is measured with a current preamplifier (SRS, model SR570). The resulting image is the convolution of the point spread function of the laser with the intrinsic region of the CNT pn junction (Fig. 1c,d). The spot size of the focused laser is determined by fitting Gaussian profiles to the parallel and perpendicular axes of the photocurrent spot.

To submerge the CNT in oil, a grounded metal wire (a clean paperclip attached to a grounding cord) was dipped in oil. Oil was then transferred from the oil-coated paper clip to the device chip. The oil wetted the SiO₂ surface, forming a thin layer across the entire device.

Approximately 90% of suspended CNT devices survive this process. If the paper clip is not grounded, only 10% of suspended CNT devices survive the process.

The chirality of the CNT is identified with spectrally resolved SPCM. 17,19,28,34,35 Photocurrent spectra were obtained by aligning the laser on the CNT pn junction, defocusing the spot, and measuring photocurrent while tuning the monochromator setting. The incident laser power is simultaneously recorded (Thorlabs PM100USB with S120C for 400-1000 nm or SC122 for 1000 – 1800 nm) by splitting the beam ahead of the objective. The ratio of power transmitted through the objective to power transmitted to the power meter is characterized before the experiment. The defocused spot size, $A_{\rm spot}$ is determined by comparing the magnitude of photocurrent produced by the CNT when the laser is defocused to the photocurrent magnitude in the imaging configuration (where the spot area is known). The chiral indices of the CNT are determined by measuring the exciton resonance energies and comparing these energies to atlas data. 17 The chirality of the CNT used in this study was determined to be (22,6), with D = 2.0 nm and a bandgap $E_{\rm G} \approx 0.5$ eV.

The graphene is suspended on devices *via* a semi-dry transfer process.³⁶ We obtain pristine CVD-grown, single-layer, graphene on copper sheets (Graphena). The graphene is coated in a negative photoresist (AZ1512) which is patterned on the foil into a grid of 40 µm bars with 16 µm pitch using standard photolithographic techniques. Once the photoresist is developed, the exposed graphene is etched in an Ar plasma for 10 seconds. Etching the graphene into bars before transferring limits electrical shorting on the chip. The patterned graphene foil is coated in 3 µm thick 950K poly(methyl methacrylate) (PMMA). A piece of thermal-release tape, with a hole cut in the middle, is used as a frame to support the PMMA. The tape/PMMA/graphene/Cu stack is floated on copper etchant (Transene) overnight to dissolve the copper. The stack is then rinsed in subsequent water baths, and air dried overnight. The stack is placed on the chip and left on a hotplate at ~180°C overnight to relax wrinkles in the graphene. The frame of thermal release tape is removed (using a scalpel to cut the PMMA where it meets the frame). The residual PMMA is burned off in a gas-flow furnace at 400°C in a H₂/Ar environment. This leaves the patterned graphene all over the chip, with some sheets bridging gaps between electrodes on either side of the trenches on our device (see Figure 2a, b). More details of the

device fabrication are given in S.I. Spectra from the incandescent graphene sheet were captured with a fiber optic spectrometer (Ocean Insight, model USB4000).

SUPPORTING INFORMATION

Electrical and scanning photocurrent characterization of the CNT photodiode in different environments; refractive index determination for the oil environment; details of self-consistent field calculations and FDTD calculations; chiral identification of CNTs; graphene device fabrication and characterization, and spectral calibration; strain and Stark effect analysis; calculations of the S_{22} linewidth under electric field in dielectrics; calculation of the height change of the CNT under gate voltage; comparison of measured photocurrent quantum yield to a carrier-escape-time model; supporting quantum yield data for Devices 1, 2, and 3.

CONFLICT OF INTEREST

The authors declare no competing financial interest.

ACKNOWLEDGEMENT

This material is based upon work supported by the National Science Foundation under Grant No. 1709800. A portion of device fabrication was carried out in the University of California Santa Barbara (UCSB) nanofabrication facility. Part of this research was conducted at the Northwest Nanotechnology Infrastructure, a National Nanotechnology Coordinated Infrastructure site at Oregon State University which is supported in part by the National Science Foundation (grant NNCI-1542101) and Oregon State University. We thank D. McCulley, D. Miller, B. Carter, and B. Alemán for valuable discussions and C. Fengel for fabrication assistance with graphene devices.

REFERENCES

- (1) Gabor, N. M.; Zhong, Z.; Bosnick, K.; Park, J.; McEuen, P. L. Extremely Efficient Multiple Electron-Hole Pair Generation in Carbon Nanotube Photodiodes. *Science*. **2009**, 325, 1367–1371.
- (2) Kumamoto, Y.; Yoshida, M.; Ishii, A.; Yokoyama, A.; Shimada, T.; Kato, Y. K. Spontaneous Exciton Dissociation in Carbon Nanotubes. *Phys. Rev. Lett.* **2014**, *112*,

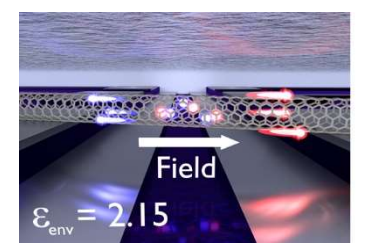
- 117401.
- (3) Wang, F.; Wang, S.; Yao, F.; Xu, H.; Wei, N.; Liu, K.; Peng, L. M. High Conversion Efficiency Carbon Nanotube-Based Barrier-Free Bipolar-Diode Photodetector. *ACS Nano* **2016**, *10*, 9595–9601.
- (4) McCulley, D. R.; Senger, M. J.; Bertoni, A.; Perebeinos, V.; Minot, E. D. Extremely Efficient Photocurrent Generation in Carbon Nanotube Photodiodes Enabled by a Strong Axial Electric Field. *Nano Lett.* **2020**, *20*, 433–440.
- (5) Baer, R.; Rabani, E. Can Impact Excitation Explain Efficient Carrier Multiplication in Carbon Nanotube Photodiodes? *Nano Lett.* **2010**, *10*, 3277–3282.
- (6) Ohno, Y.; Iwasaki, S.; Murakami, Y.; Kishimoto, S.; Maruyama, S.; Mizutani, T. Excitonic Transition Energies in Single-Walled Carbon Nanotubes: Dependence on Environmental Dielectric Constant. *Phys. status solidi* **2007**, *244*, 4002–4005.
- (7) Choi, J. H.; Strano, M. S. Solvatochromism in Single-Walled Carbon Nanotubes. *Appl. Phys. Lett.* **2007**, *90*, 88–91.
- (8) Walsh, A. G.; Nickolas Vamivakas, A.; Yin, Y.; Cronin, S. B.; Goldberg, B. B.; Unlu, S.; Swan, A. K. Screening of Excitons in Single, Suspended Carbon Nanotubes. *Nano Lett.* 2007, 7, 1485-1488.
- (9) Uda, T.; Tanaka, S.; Kato, Y. K. Molecular Screening Effects on Exciton-Carrier Interactions in Suspended Carbon Nanotubes. *Appl. Phys. Lett.* **2018**, *113*, 1–4.
- (10) Tanaka, S.; Otsuka, K.; Kimura, K.; Ishii, A.; Imada, H.; Kim, Y.; Kato, Y. K. Organic Molecular Tuning of Many-Body Interaction Energies in Air-Suspended Carbon Nanotubes. J. Phys. Chem. C 2019, 123, 5776–5781.
- (11) Fang, N.; Otsuka, K.; Ishii, A.; Taniguchi, T.; Watanabe, K.; Nagashio, K.; Kato, Y. K. Hexagonal Boron Nitride as an Ideal Substrate for Carbon Nanotube Photonics. *ACS Photonics* **2020**, *7*, 1773–1779.
- (12) Homma, Y.; Chiashi, S.; Yamamoto, T.; Kono, K.; Matsumoto, D.; Shitaba, J.; Sato, S. Photoluminescence Measurements and Molecular Dynamics Simulations of Water Adsorption on the Hydrophobic Surface of a Carbon Nanotube in Water Vapor. *Phys. Rev. Lett.* 2013, 110, 1–4.
- (13) Stier, A. V.; Wilson, N. P.; Clark, G.; Xu, X.; Crooker, S. A. Probing the Influence of Dielectric Environment on Excitons in Monolayer WSe₂: Insight from High Magnetic

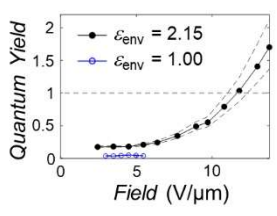
- Fields. Nano Lett. 2016, 16, 7054-7060.
- (14) Raja, A.; Chaves, A.; Yu, J.; Arefe, G.; Hill, H. M.; Rigosi, A. F.; Berkelbach, T. C.; Nagler, P.; Schüller, C.; Korn, T.; Nuckolls, C.; Hone, J.; Brus, L. E.; Heinz, T. F.; Reichman, D. R.; Chernikov, A. Coulomb Engineering of the Bandgap and Excitons in Two-Dimensional Materials. *Nat. Commun.* **2017**, *8*, 1–7.
- (15) Park, S.; Mutz, N.; Schultz, T.; Blumstengel, S.; Han, A.; Aljarb, A.; Li, L. J.; List-Kratochvil, E. J. W.; Amsalem, P.; Koch, N. Direct Determination of Monolayer MoS₂ and WSe₂ Exciton Binding Energies on Insulating and Metallic Substrates. *2D Mater*. **2018**, *5*, 025003.
- (16) Waldecker, L.; Raja, A.; Rösner, M.; Steinke, C.; Bostwick, A.; Koch, R. J.; Jozwiak, C.; Taniguchi, T.; Watanabe, K.; Rotenberg, E.; Wehling, T. O.; Heinz, T. F. Rigid Band Shifts in Two-Dimensional Semiconductors through External Dielectric Screening. *Phys. Rev. Lett.* **2019**, *123*, 206403.
- (17) Liu, K.; Deslippe, J.; Xiao, F.; Capaz, R. B.; Hong, X.; Aloni, S.; Zettl, A.; Wang, W.; Bai, X.; Louie, S. G.; Wang, E.; Wang, F. An Atlas of Carbon Nanotube Optical Transitions. *Nat. Nanotechnol.* 2012, 7, 325–329.
- (18) Ando, T. Effects of Environmental Dielectric Screening on Optical Absorption in Carbon Nanotubes. *Phys. E Low-Dimensional Syst. Nanostructures* **2011**, *43*, 798–803.
- (19) Aspitarte, L.; McCulley, D. R.; Minot, E. D. Photocurrent Quantum Yield in Suspended Carbon Nanotube *p-n* Junctions. *Nano Lett.* **2016**, *16*, 5589–5593.
- (20) Lumerical Inc. FDTD. https://www.lumerical.com/products/fdtd (accessed December 11, 2019).
- (21) Nair, R. R.; Blake, P.; Grigorenko, A. N.; Novoselov, K. S.; Booth, T. J.; Stauber, T.; Peres, N. M. R.; Geim, A. K. Fine Structure Constant Defines Visual Transparency of Graphene. *Science.* 2008, 320, 1308.
- (22) Kim, Y. D.; Kim, H.; Cho, Y.; Ryoo, J. H.; Park, C. H.; Kim, P.; Kim, Y. S.; Lee, S.; Li, Y.; Park, S. N.; Shim Yoo, Y.; Yoon, D.; Dorgan, V. E.; Pop, E.; Heinz, T. F.; Hone, J.; Chun, S. H.; Cheong, H.; Lee, S. W.; Bae, M. H.; *et al.* Bright Visible Light Emission from Graphene. *Nat. Nanotechnol.* **2015**, *10*, 676–681.
- (23) Perebeinos, V.; Avouris, P. Exciton Ionization, Franz-Keldysh, and Stark Effects in Carbon Nanotubes. *Nano Lett.* **2007**, *7*, 609–613.

- (24) Huang, M.; Wu, Y.; Chandra, B.; Yan, H.; Shan, Y.; Heinz, T. F.; Hone, J. Direct Measurement of Strain-Induced Changes in the Band Structure of Carbon Nanotubes. *Phys. Rev. Lett.* **2008**, *100*, 1–4.
- (25) Irvine, H. M. *Cable Structures*; MIT Press Series in Structural Mechanics; MIT Press: Cambridge, Mass., 1981.
- (26) Yasukochi, S.; Murai, T.; Moritsubo, S.; Shimada, T.; Chiashi, S.; Maruyama, S.; Kato, Y. K. Gate-Induced Blueshift and Quenching of Photoluminescence in Suspended Single-Walled Carbon Nanotubes. *Phys. Rev. B Condens. Matter Mater. Phys.* **2011**, *84*, 1–4.
- (27) Wang, F.; Dukovic, G.; Knoesel, E.; Brus, L. E.; Heinz, T. F. Observation of Rapid Auger Recombination in Optically Excited Semiconducting Carbon Nanotubes. *Phys. Rev. B Condens. Matter Mater. Phys.* **2004**, *70*, 1–4.
- (28) Liu, K.; Hong, X.; Choi, S.; Jin, C.; Capaz, R. B.; Kim, J.; Wang, W.; Bai, X.; Louie, S. G.; Wang, E.; Wang, F. Systematic Determination of Absolute Absorption Cross-Section of Individual Carbon Nanotubes. *Proc. Natl. Acad. Sci.* 2014, 111, 7564–7569.
- (29) Hertel, T.; Perebeinos, V.; Crochet, J.; Arnold, K.; Kappes, M.; Avouris, P. Intersubband Decay of 1-D Exciton Resonances in Carbon Nanotubes. *Nano Lett.* **2008**, *8*, 87–91.
- (30) Chen, J.; Perebeinos, V.; Freitag, M.; Tsang, J.; Fu, Q.; Liu, J.; Avouris, P. Bright Infrared Emission from Electrically Induced Excitons in Carbon Nanotubes. *Science*. **2005**, *310*, 1171 LP 1174.
- (31) Perebeinos, V.; Avouris, P. Impact Excitation by Hot Carriers in Carbon Nanotubes. *Phys. Rev. B Condens. Matter Mater. Phys.* **2006**, *74*, 1–4.
- (32) Okuto, Y.; Crowell, C. R. Energy-Conservation Considerations in the Characterization of Impact Ionization in Semiconductors. *Phys. Rev. B* **1972**, *6*, 3076–3081.
- (33) Sharf, T.; Kevek, J. W.; Minot, E. D. Fabrication of Low-Noise Carbon Nanotube Field-Effect Transistor Biosensors. In *Nanotechnology (IEEE-NANO)*, Proceedings of the 2011 11th IEEE International Conference on Nanotechnology, Portland, Oregon, USA, August 15-18, 2011; IEEE: Portland, Oregon, 2011; 122–125.
- (34) Deborde, T.; Aspitarte, L.; Sharf, T.; Kevek, J. W.; Minot, E. D. Determining the Chiral Index of Semiconducting Carbon Nanotubes Using Photoconductivity Resonances. *J. Phys. Chem. C* **2014**, *118*, 9946–9950.
- (35) Senger, M. J.; McCulley, D. R.; Lotfizadeh, N.; Deshpande, V. V.; Minot, E. D. Universal

- Interaction-Driven Gap in Metallic Carbon Nanotubes. Phys. Rev. B 2018, 97, 035445.
- (36) Suk, J. W.; Kitt, A.; Magnuson, C. W.; Hao, Y.; Ahmed, S.; An, J.; Swan, A. K.; Goldberg, B. B.; Ruoff, R. S. Transfer of CVD-Grown Monolayer Graphene onto Arbitrary Substrates. *ACS Nano* **2011**, *5*, 6916–6924.

FOR TABLE OF CONTENTS ONLY





Supporting Information for:

Dielectric Engineering Boosts the Efficiency of Carbon Nanotube Photodiodes

Mitchell J. Senger, † Ali Kefayati, § Andrea Bertoni, ‡ Vasili Perebeinos, § Ethan D. Minot†, *

1. CNT Electrical Characterization in Oil / Vacuum

CNT devices were electrically characterized in a transistor configuration ($V_G = V_{G1} = V_{G2}$), and a diode configuration ($V_{G1} = -V_{G2}$). In the $I(V_G)$ curve of the transistor, we see a sharp turn on near $V_G = 0$ V and p-type conduction. When the device is submerged in oil, the transistor $I(V_G)$ curve is almost identical. In the diode configuration, the diode rectifies in reverse bias, and turns on sharply near $V_{SD} = 1$ V. The diode ideality is ~ 1.2 in air and is retained in the oil environment.

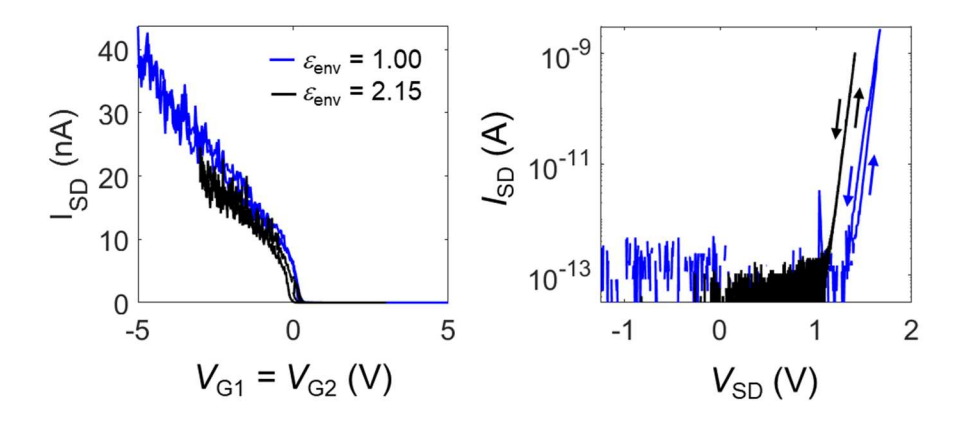


Figure S1. a) Current vs. gate voltage ($V_{\rm G1} = V_{\rm G2}$) of Device 1 in air, and in oil. The source-drain voltage is 25 mV. b) $I(V_{\rm SD})$ measurements for the device in vacuum ($V_{\rm G1} = -V_{\rm G2} = 5\rm V$) and in oil ($V_{\rm G1} = -V_{\rm G2} = 4\rm V$). The diode turn-on in vacuum occurs at a larger $V_{\rm SD}$ than in oil because of the different gate voltage settings.¹

[†]Department of Physics, Oregon State University, Corvallis, Oregon 97331, United States,

[§]Department of Electrical Engineering, University at Buffalo, The State University of New York, Buffalo, NY 14260, United States,

[‡]Istituto Nanoscienze-CNR, Via Campi 213a, I-41125 Modena, Italy

2. Vacuum Pump Oil Refractive Index and DC Dielectric Constant Determination

The refractive index of the HyVac vacuum pump oil ($n_{\text{oil}} = 1.4793 \pm 0.0001$) was measured at a wavelength $\lambda = 600$ nm using a digital Abbe refractometer (Leica Mark II). To estimate the refractive index at longer wavelengths, we use the Cauchy equation²

$$n(\lambda) = n_0 + \frac{c_1}{\lambda^2} + \frac{c_2}{\lambda^4}.$$

Following Ref. 2, we approximate the Cauchy constants as $n_0 = 1.466$, $c_1 = 0.005 \,\mu\text{m}^2$, and $c_2 = -0.0001 \,\mu\text{m}^4$. For FDTD calculations we use n = 1.470 when studying the S_{22} resonance of Device 1 ($\lambda = 1305 \,\text{nm}$) and n = 1.476 when studying the S_{33} resonance of Devices 2 and 3 ($\lambda = 710 \,\text{nm}$ and $\lambda = 640 \,\text{nm}$, respectively). For electrostatics and electromechanical modeling, we use the DC dielectric constant which we calculate as $\varepsilon_{\text{env}} = n_0^2 = 2.15$.

3. Self-Consistent Field Calculations

The self-consistent field (SCF) calculations were used to find the intrinsic region length of the CNT *pn* junction and the electric field strength inside the intrinsic region. The calculation method was previously described by McCulley *et al.*³ Figure S2 shows the charge density on the CNT, the intrinsic region, and self-consistent energy bands for several voltage settings.

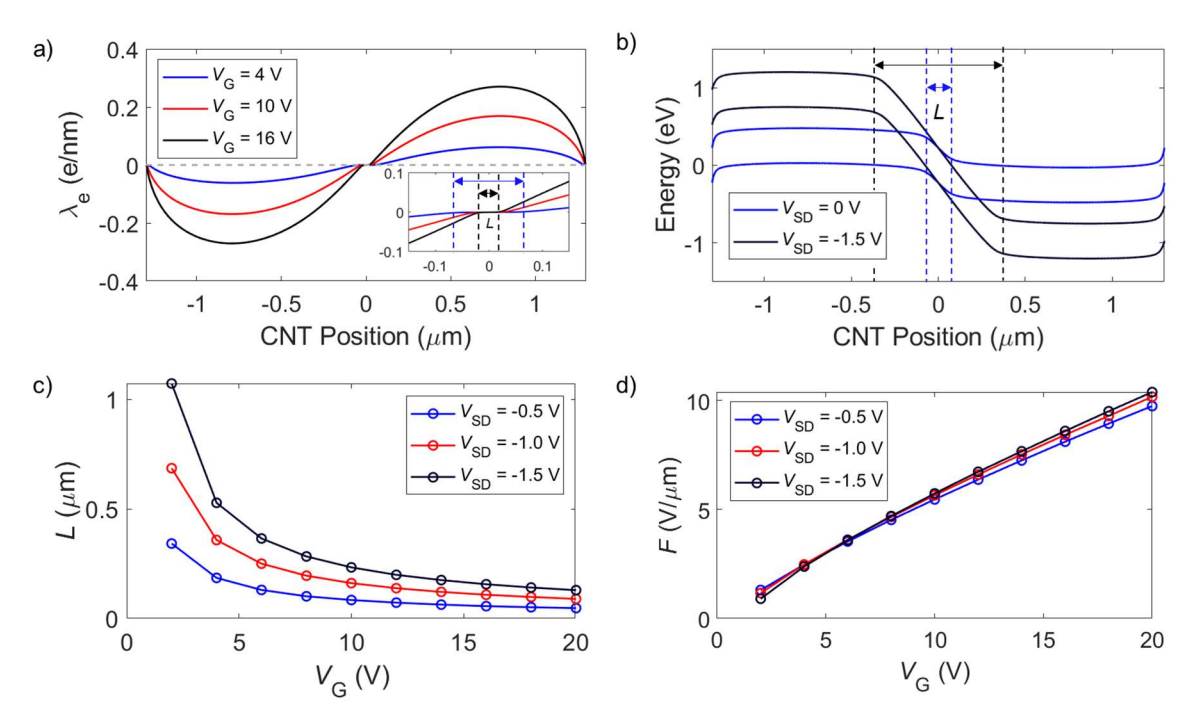


Figure S2. Results of self-consistent field calculations for the CNT pn junction in vacuum. a) Linear charge density, λ_e , along the length of the CNT at zero bias. $V_{G1} = -V_{G2} = V_G$. The length of the intrinsic region in the pn junction, L, is determined by the length of the region where $\lambda_e < 6.25 \times 10^{-6}$ electrons per nanometer. Inset: $\lambda_e(x)$ zoomed in near the origin. Increasing gate voltage shrinks the intrinsic region. b) Conduction and valance band energy along the length of the CNT at $V_G = V_{G1} = -V_{G2} = 4$ V. Increasing the bias magnitude increases L but leaves the slope of the bands mostly unchanged. c) L against V_G . d) Maximum value of electric field, F, in the pn junction against V_G . The bias has a negligible effect on the magnitude of F.

The field strength, F, and length of the intrinsic region, L, are not changed by the dielectric constant of the environment. We explain this result as follows. Firstly, the external field produced by the electrodes is not changed by the dielectric environment (the voltage boundary conditions for the Poisson equation are unchanged). Secondly, the charge density, λ_e , is increased when the CNT pn junction is submerged in oil (the capacitance between the gate electrodes and the CNT is increased by a factor ε_{env}). However, the internal field produced by λ_e is screened by the dielectric environment, also by a factor ε_{env} . Figure S3 shows the SCF calculation of L when $\varepsilon_{env} = 1$ and $\varepsilon_{env} = 3$. The $L(V_G)$ curves are nearly identical.

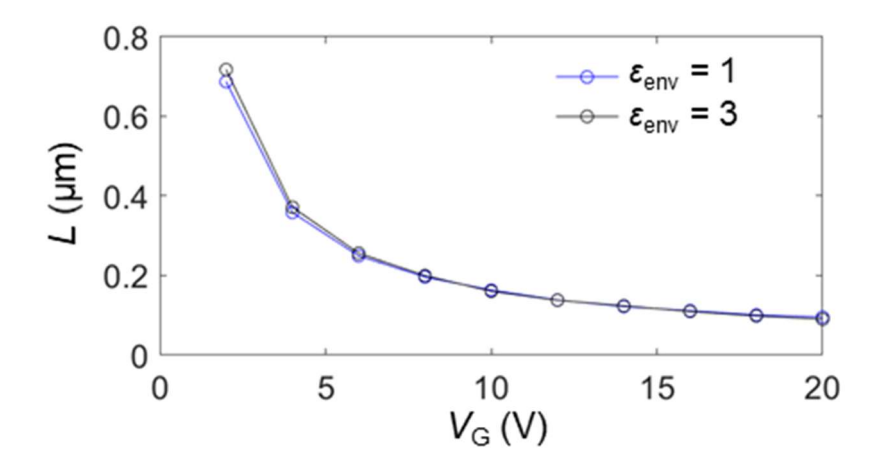


Figure S3. Self-consistent intrinsic region length calculated for the CNT when $\varepsilon_{\rm env} = 1$ (blue) and in dielectric material (black) with $\varepsilon_{\rm env} = 3$. $V_{\rm G} = V_{\rm G1} = -V_{\rm G2}$ and $V_{\rm SD} = -1$ V.

4. Scanning Photocurrent Microscopy

The device is illuminated with a supercontinuum laser filtered by a double monochromator to a \sim 5 nm linewidth. The laser was focused to the plane of the CNT and rastered over the sample via a pair of computer-controlled galvo mirrors. The photocurrent, I_{PC} , is recorded as a function of laser position using a current preamplifier (SR570). Figure S4 shows scanning photocurrent microscope (SPCM) images of Device 1 in oil in different electrical configurations. With zero gate voltage and zero bias, the Schottky barriers at the contacts produce photocurrent (Figure S4a). A pn junction is induced in the device, SPCM shows one active region at the center of the device (Figure S4b). In this voltage configuration, the zero-intensity current is close to zero (see Figure S1b), so the current in the image is coming only from photoexcited carriers. When the reverse bias is increased (Figure S4c), the magnitude of the photocurrent increases because the intrinsic region is lengthened (see Figure S2b). All spectral photocurrent data is taken under a reverse bias.

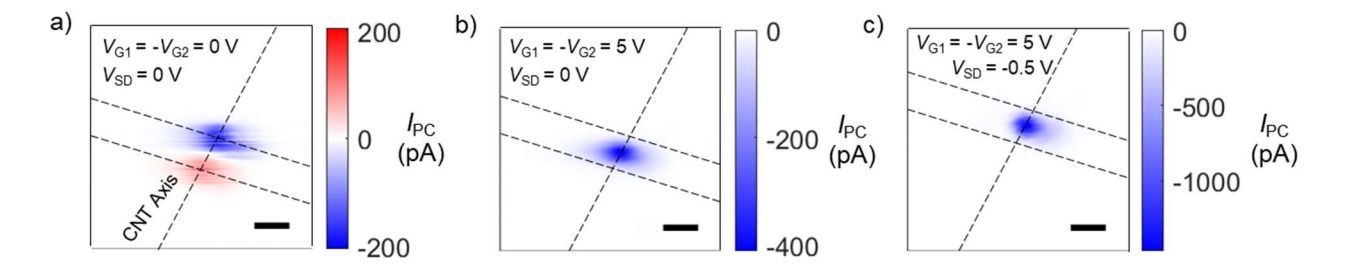


Figure S4. SPCM images of the Device 1 in oil with $\hbar\omega = 2.25$ eV. a) Two spots are visible due to excitation at the Schottky barriers. b) A pn junction is generated in the center of the CNT with the split gates. c) The photocurrent magnitude at the pn junction is increased by applying a bias. All scale bars are 2 μ m.

Our SCF calculations indicate that the intrinsic region length (L) depends on the gate electrode voltage ($V_G = V_{G1} = -V_{G2}$) and the source drain bias (V_{SD}). Figure S5 shows SPCM images of the CNT in oil taken at the $V_G = 4$ V using a laser spot with a point spread width ≈ 600 nm. Increasing $|V_{SD}|$ past 1 V lengthens the photocurrent spot along the axis of the CNT. The magnitude of the photocurrent signal increases over the range of V_{SD} applied. We attribute this to an increase in L due to the increased bias, consistent with our SCF modeling.

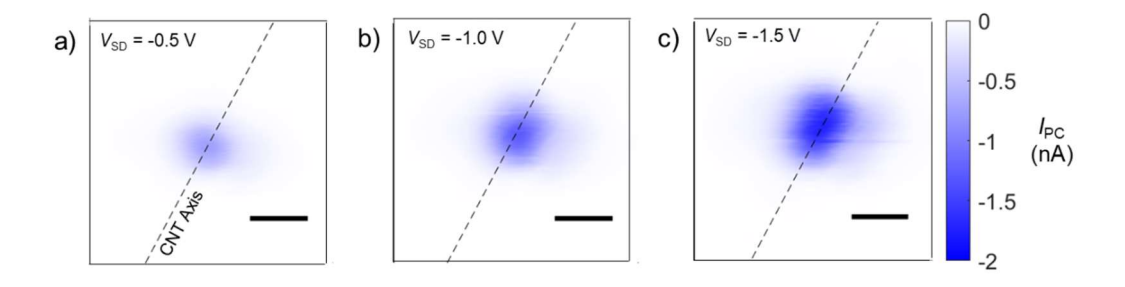


Figure S5. SPCM images of the CNT pn junction in oil using $\hbar\omega = 2.67$ eV and with $V_G = 4$ V and a) $V_{SD} = -0.5$ V, b) $V_{SD} = -1.0$ V, and c) $V_{SD} = -1.5$ V. The photocurrent spot lengthens along the CNT axis due to increasing intrinsic region. Scale bars are 1.5 μ m.

We also confirmed the linear relationship between L and $V_{\rm SD}$ by measuring photocurrent, $I_{\rm PC}$, while varying $V_{\rm SD}$ at higher fields. Figure S6 shows a photocurrent measurement of Device 1 with $V_{\rm G}=15$ V and with laser illuminated with $\hbar\omega=0.932$ eV in oil. When the reverse bias is increased, the photocurrent magnitude increases linearly in the range -0.5 V < $V_{\rm SD}$ < 0. We fit $I_{\rm PC}(V_{\rm SD})$ with the form $I=\kappa(V_{\rm SD}-V_0)$, where $\kappa=-7$ pA/V and $V_0=0.3$ V are fitting parameters.

The linearity of $I_{PC}(V_{SD})$ in the reverse bias regime corroborates the relationship $L = (E_G/e - V_{SD})$ / F introduced in the main text.

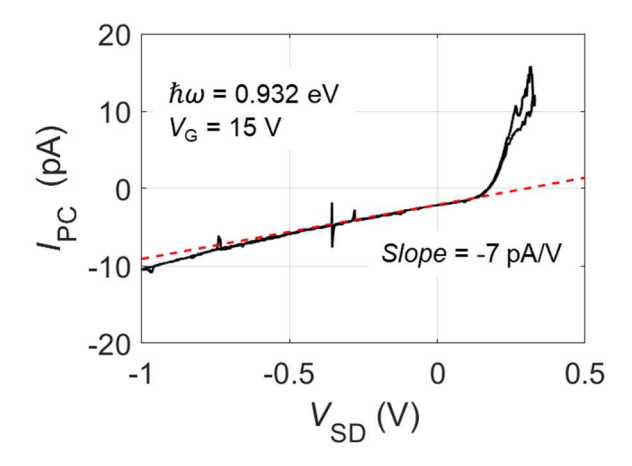


Figure S6. Bias dependent photocurrent from Device 1 in oil when it is illuminated with a defocused laser spot with $\hbar\omega = 0.932$ eV. The split gates are set to $V_G = V_{G1} = -V_{G2} = 15$ V. The red dashed line is a linear fit in the range -0.5 V < V_{SD} < 0.

5. FDTD Simulations

For a course-grained model of optical interference we considered a plane wave, $E_S = \bar{E} \exp[i(2\pi z/\lambda - \omega t)]$, incident on a reflective surface. If the substrate has a reflection coefficient, $r = r_0 e^{i\phi}$, then

$$\gamma = 1 + r_0^2 + 2r_0 \mathrm{cos}[4\pi h/\lambda - \phi].$$

The actual interference pattern will deviate from this plane wave approximation due to several factors (i) the substrate is not homogenous, (ii) the incident light is focused by a microscope objective (not a plane wave), (iii) the reflection coefficient is a function of wavelength. An SEM image of the cross section of the CNT device's substrate is shown in Figure S7a. The image shows that the substrate floor comprises split platinum gates buried in SiO_2 , which are separated by 350 nm. The distance, h, between a point level with the top of source and drain, and halfway between them, and the top of the gate electrodes is 650 nm.

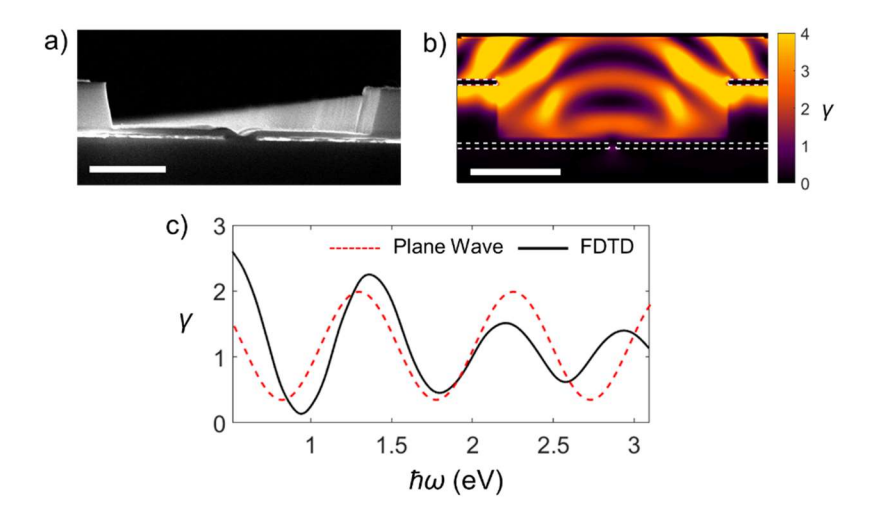


Figure S7. FDTD modeling of the substrate. a) Profile SEM image of the substrate diced through the source and drain electrodes. The metal gates buried in SiO₂ are visible. B) γ modeled with FDTD software using the substrate geometry with $\lambda_{\text{source}} = 930$ nm. White dashes outline the electrodes and the gates. Scale bars are 1 μ m. c) Intensity enhancement at the center of the CNT pn junction when the CNT is level with the top of the electrodes. Red dashed line is the plane-wave approximation, with $r_0 = 0.41$ and $\phi = 4.01$ (r_0 and ϕ were chosen to approximate the FDTD simulation).

To model the optical field more precisely, we used finite-difference time-domain software (Lumerical FDTD).⁴ In the simulation, spatial regions are assigned spectrally-defined refractive indices that correspond to the materials in the device (Pt, SiO₂, Si) are defined in a 2d plane.⁵ To model the light source, a multi-wavelength beam with numerical aperture, NA = 0.8, is directed downward at the substrate so that the minimum beam waist is located at the top of the electrodes. $|E|^2$ is calculated everywhere in space by numerically solving Maxwell's equations in the time domain. The wavelength dependence of the squared electric field is recovered with a Fourier transform. γ is calculated by normalizing $|E|^2$ with $|E_0|^2$, which is calculated by running the same simulation with a fictional device with zero reflection. A spatial map of γ from the FDTD simulations is shown in Figure S7b. The device electrodes are outlined by white dashed lines. Figure S7c shows the spectral variation in γ at the center of the CNT (in the center of the trench, level with the source and drain electrodes).

6. CNT Resting Height and Chiral Identification

Figure 3e and f of the main text show the intensity enhancement factor (γ) is sensitive to the distance between the CNT and the gates. Therefore, it is important to determine the CNT's vertical height above the gates, h. When a CNT bridges the gap between the source and drain electrode, the CNT is not always level with the top of the source and drain electrode. Figure S8 shows a scanning electron microscopy image of a CNT in one of our devices that goes part way down the trench wall before it crosses the trench and contacts the other electrode.

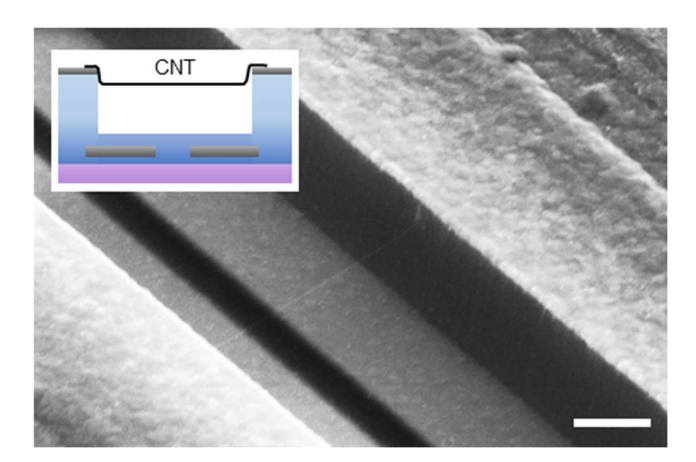


Figure S8. A scanning electron microscope image of a representative CNT suspended over the trench of a split-gate device. The CNT has grown down the trench wall 50-100 nm before bridging the trench. Scale bar is $0.5 \mu m$.

To identify the as-grown distance between the CNT and the gates, h_0 , we use a combination of spectrally-resolved photocurrent measurements, theoretical calculations of γ , and the empirical absorption cross section of the CNT, α . We identify the chirality of the CNT, which is necessary to accurately describe α , with spectral photocurrent measurements as well. Photocurrent measurements are made as described in the main text, with the gate voltages set to ~ 5 V. The wavelength of the laser is swept from 400 nm to 1000 nm. For CNTs with diameter $D \sim 2$ nm, several exciton resonances are accessible in this range of wavelengths. Figure S9d shows the photocurrent spectrum (I_{PC}) for Device 1 as measured in air normalized for the laser power (P) and the photon energy ($\hbar\omega$). The location of the photocurrent peaks at $\hbar\omega = 1.70$ eV, 2.34 eV, and 2.67 eV, correspond to the S_{33} , S_{44} , and S_{55} transitions of the CNT. These exciton energies are consistent with a CNT with chirality (22,6).

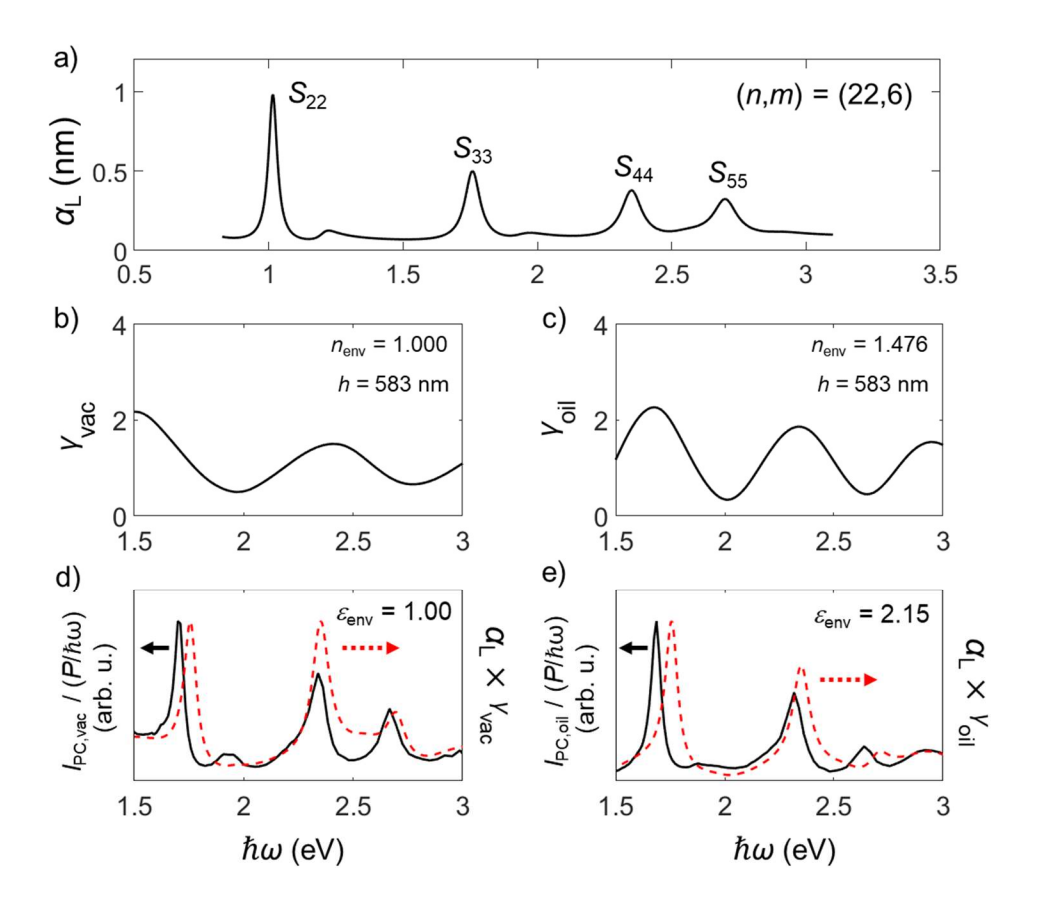


Figure S9. Finding the CNT chirality and as-grown height. a) The empirical absorption cross section per length of a CNT with chirality (22, 6).^{6,7} b) γ calculated in FDTD simulations for a vacuum environment using $h_0 = 583$ nm. c) γ calculated in FDTD simulations for the oil environment using $h_0 = 583$ nm. d) Photocurrent spectrum measured in air normalized for $P/\hbar\omega$ (black) plotted along with $\gamma_{\rm vac}\alpha_{\rm L}$ (red dashes) where $\gamma_{\rm vac}$ is calculated using $h_0 = 583$ nm. e) Photocurrent spectrum measured in the oil environment normalized for $P/\hbar\omega$ (black) plotted along with $\gamma_{\rm oil}\alpha_{\rm L}$ (red dashes) where $\gamma_{\rm oil}$ is calculated using $h_0 = 583$ nm.

The absorption cross section, α , for this CNT is calculated in the scheme presented by Wang *et al.*^{6,7} In this scheme, α has dimensions of area per atom. We are interested in the differential oscillator strength per length of the CNT, α L, which we calculate as

$$\alpha_{\rm L} = \alpha N_{\rm L}$$
.

 $N_{\rm L}$ is the number of atoms per length of the CNT, given by $N_{\rm L}=4\pi D/\sqrt{3}a^2$, where a=0.246 nm is the graphene unit vector length. For a nanotube with chirality (22,06), $N_{\rm L}=239.7$ atoms/nm. The spectral photocurrent magnitude is proportional to $P\gamma\alpha_{\rm L}/\hbar\omega$. We compare the photocurrent

normalized for laser power and photon energy $(I_{PC}/(P/\hbar\omega))$ to $\gamma\alpha_L$, as shown in Figure S9d,e. h is varied until $\gamma\alpha_L$ closely matches $I_{PC}/(P/\hbar\omega)$ in both environments. For Device 1, we find a good match between the two curves when $\gamma\alpha_L$ is calculated using $h_0 = 583$ nm, as shown in Figure S9d and e.

7. Graphene Device Fabrication

The graphene is suspended on our devices *via* a semi-dry transfer process first developed by Suk *et al.*⁸ We obtain pristine CVD-grown, single-layer, graphene on copper sheets (Graphena). The graphene is coated in a negative photoresist (AZ1512) which is patterned on the foil into a grid of 40 µm bars with 16 µm pitch using standard photolithographic techniques. Once the photoresist is developed, the exposed graphene is etched *via* mechanical bombardment in an Ar plasma for 10 seconds. The resist is removed in a Remover PG (Microchem) bath. Etching the graphene into bars before transferring it allows us to place the entire foil of graphene to the device with limited electrical shorting. The patterned graphene foil is then coated in 3 µm deep 950K poly(methyl methacrylate) (PMMA). A sheet of thermal tape, hole-punched through the center to leave the PMMA/graphene stack that will rest on the device undisturbed, is layered on the PMMA for structural reinforcement. The tape/PMMA/graphene/Cu stack is floated on a Cu etchant (Transene) bath overnight to dissolve the foil. The stamp is then removed, rinsed in subsequent water baths, and air dried overnight.

The graphene stamp is then placed on the chip and left on a hotplate at $\sim 180^{\circ}$ C overnight, allowing wrinkles in the PMMA to relax and the graphene to rest levelly over the trenches on the chip. Finally, the PMMA is cut from the tape and the residual PMMA is burned off in a gas-flow furnace at 400°C in a H₂/Ar environment. This leaves the patterned graphene all over the chip, with some sheets bridging gaps between electrodes on either side of the trenches on our device (see Figure 2 in the main text).

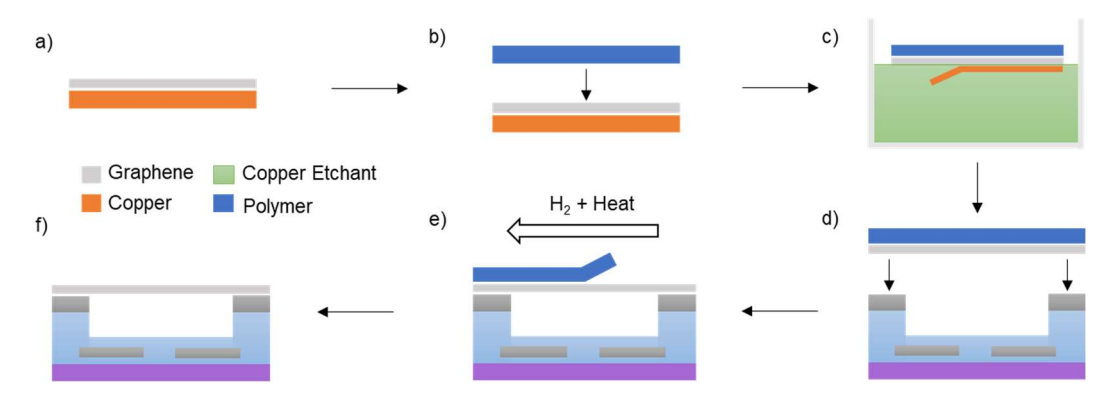


Figure S10. Fabrication steps to build a suspended graphene device: a) Graphene is deposited onto a copper foil with CVD techniques and patterned into a desirable shape using photolithographic techniques and dry mechanical etching. b) PMMA polymer is spin cast onto the sample. c) The copper foil is dissolved in an appropriate etchant. The stamp is washed in water and dried. d) The stamp is placed on the final device substrate. e) The polymer is removed in a H₂/Ar atmosphere using a CVD furnace. f) The final device is the same as the CNT devices, but the graphene monolayer is in the CNT's place.

After fabrication is complete, the device is wire bonded, loaded into an optical cryostat (Janis), and brought to vacuum ($< 10 \mu Torr$). The device is biased with a source drain voltage, V_{SD} , and the current, I, is measured with a preamplifier (Stanford Research). A typical $I(V_{SD})$ of a suspended graphene device is shown in Figure S11. Incandescence was easily observable when V_{SD} was approximately 4 V.

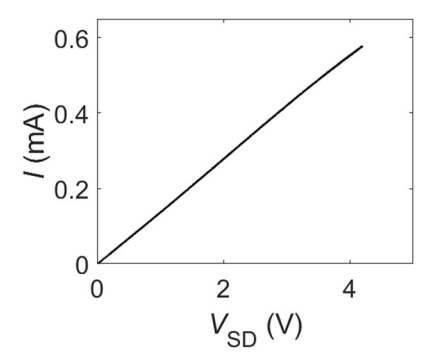


Figure S11. Typical $I(V_{SD})$ characterization of a suspended graphene device. The channel length is 2.6 µm and channel width ~15 µm. Incandescence for this device was visible when $V_{SD} = 4.1 \text{ V}$.

8. Determining the Spectrometer Efficiency Curve

The spectrum from the incandescent graphene sheet is measured with a visible-light fiber optic spectrometer (Ocean Insight). Figure S12c shows the spectrometer's spectral efficiency curve $(\rho(\lambda))$ determined by referencing an incandescent lightbulb spectrum, S_{LB} , at $T \approx 2200$ K. The spectral irradiance (I) of the lightbulb is modeled with a blackbody with T = 2200 K. I is calculated using Planck's law

$$I(\lambda,T) = 2\pi \frac{hc^2}{\lambda^5} \frac{1}{\exp\left(\frac{hc}{k_BT\lambda}\right)-1},$$

where h is Planck's constant, c is the speed of light, and k_B is Boltzmann's constant. The efficiency is calculated as

$$\rho(\lambda) = \frac{I_{2200K} / S_{LB}}{\max(I_{2200K} / S_{LB})}.$$

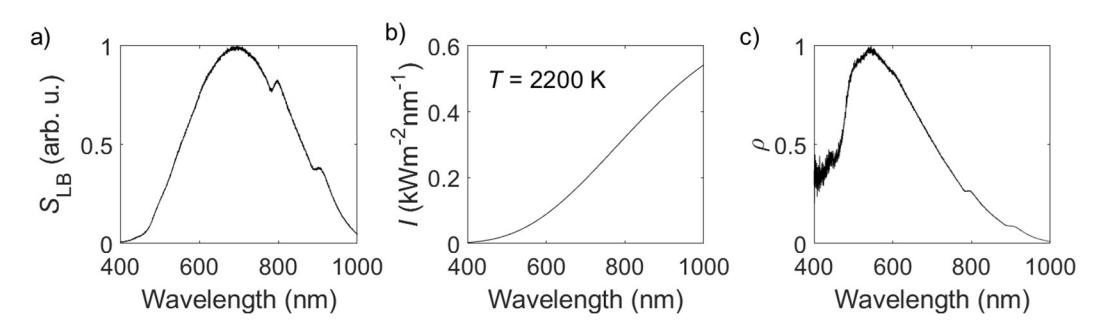


Figure S12. Determination of the spectrometer's efficiency (ρ). a) Measured spectrum from an incandescent lightbulb at 2200 K. b) Modeled black body irradiance at 2200 K. c) Spectral efficiency of the spectrometer for normalizing the incandescence spectrum collected from the graphene sheet.

To correctly identify the temperature of the graphene sheet in the main text (T = 1400 K), the temperature of the reference must be known precisely. We corroborate the efficiency curve from the lightbulb reference by also referencing the spectrometer to a Xe lamp (Newport 67005) filtered with an air mass filter (Newport 81088A), *i.e.*, a solar simulator. Figure S13 shows the measured spectrum, S_S , the modeled blackbody emissivity spectrum, and the resultant efficiency curve compared to the curve in Figure S12c.

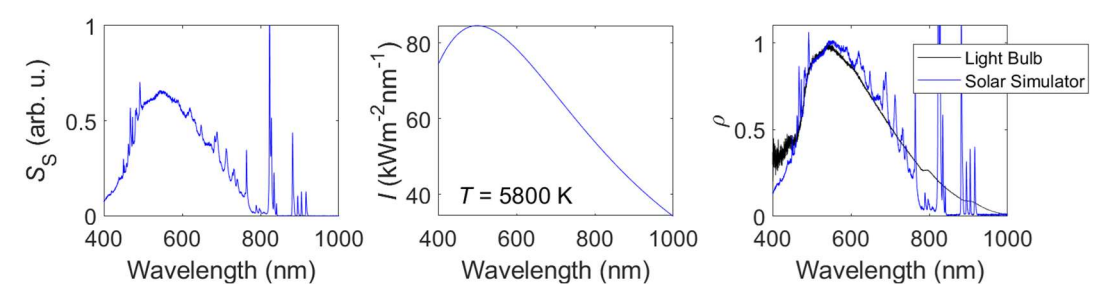


Figure S13. Determination of the spectrometer's efficiency from a solar simulator reference. a) Measured spectrum, S_S . b) Modeled black body irradiance at 5800 K. c) Spectral efficiency of the spectrometer calculated using the 2200 K lightbulb (black) and the solar simulator (blue).

The spectrum produced by the solar simulator is not smooth, and has missing wavelengths in the near IR, making it difficult calculate a smooth efficiency curve for the spectrometer. However, solar simulator measurement corroborates the efficiency curve that we calculated from the incandescent lightbulb.

9. S₃₃ Photocurrent Spectra and Peak Shift of Device 1

The energies of the S_{22} and S_{33} exciton resonances change by equal and opposite amounts when a CNT is strained. This allows us to disentangle strain-induced shifts from the Stark shift. The spectral photocurrent near S_{33} is plotted in Figure S14a for a range of gate voltages. The peak blueshifts with increased gate voltage, contrary to the redshift we found at S_{22} .

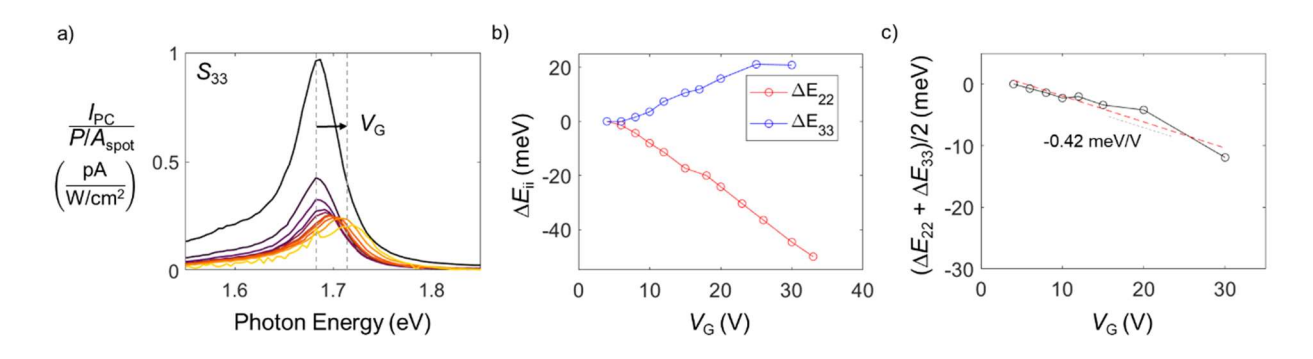


Figure S14. a) The S_{33} resonance measured with the split gate voltage going from 4 V to 30 V with the CNT in oil with $V_{SD} = -0.5$ V. b) The shift of the S_{22} and S_{33} resonances due to the applied gate voltage. c) The peak shift due to non-strain effects. The red line is a linear fit of the shift, with slope -0.42 meV/V.

Figure S14b shows the peak shift for S_{22} and S_{33} (ΔE_{22} and ΔE_{33} , respectively) as a function of gate voltage. If there was no Stark shift, we would expect $\Delta E_{22} + \Delta E_{33} = 0$. We estimate the Stark shift as ($\Delta E_{22} + \Delta E_{33}$)/2 (Figure S14c). This inferred Stark shift reaches approximately -10 meV, consistent with theory.¹⁰

10. Autoionization of S_{22} Excitons in Dielectrics

In the main text, we observe increases in η_{22} when the field is increased past 5 V/ μ m when the CNT is in dielectric oil. We also observe $\eta_{22} > 1$ when F > 11.5 V/ μ m. We attribute these behaviors to modifications in the decay channels for S_{22} from dielectric screening. To understand how the branching ratios of the S_{22} decay are modified, we calculate the FWHM of the S_{22} absorption resonance with the Bethe-Salpeter equation. Figure S15 shows the calculated FWHM of the S_{22} resonance at low field (purple) and high field (orange) as a function of the effective dielectric constant of the CNT and its environment, $\varepsilon_{\rm eff}$.

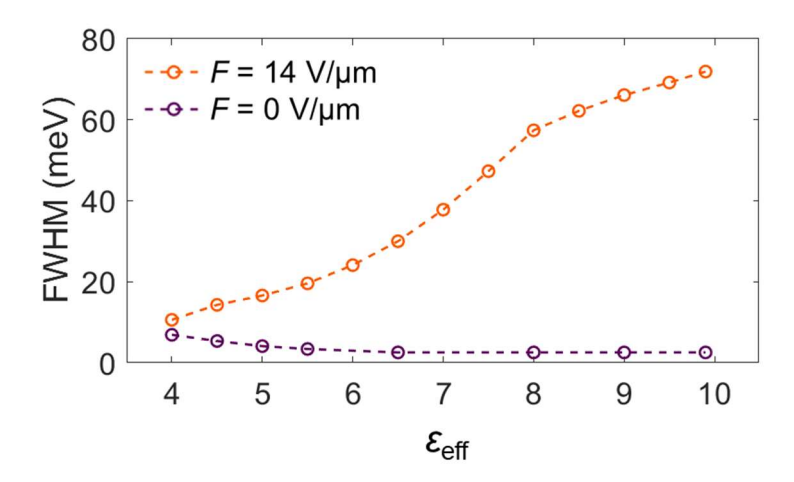


Figure S15. Calculated full-width at half maximum (FWHM) of the S_{22} resonance as a function of effective dielectric constant. At high field (orange), the fraction of autoionized excitons increases with dielectric constant leading to larger FWHM. At low field (purple), FWHM decreases with increased dielectric constant because reducing the exciton binding energy increases mixing between the S_{22} and free carrier states in the first subband.

When F = 0, the FWHM decreases with ε_{eff} (purple line). The electronic decay rate is reduced by ε_{eff} because Coulomb interactions are reduced, and because the density of the free carrier

continuum in the first subband at the S_{22} energy is reduced. In contrast, when $F = 14 \text{ V/}\mu\text{m}$, the reduced exciton binding energy increases the autoionization rate of $S_{22} \rightarrow e_2 + h_2$. The increased decay rate of S_{22} causes lifetime broadening of the exciton resonance peak (orange line in Figure S15).

11. Electromechanical Model of the Suspended CNT Under Gate Voltage

The voltage on the two gates creates an electric field that acts on charges in the CNT. These electrostatic forces cause the CNT to bend and stretch. Change in the height of the CNT affects the illumination intensity in our optoelectronics experiments. We first calculate the electrostatic potential and electric field in the absence of the CNT using a numerical Poisson solver (Figure S16a, c, and e).

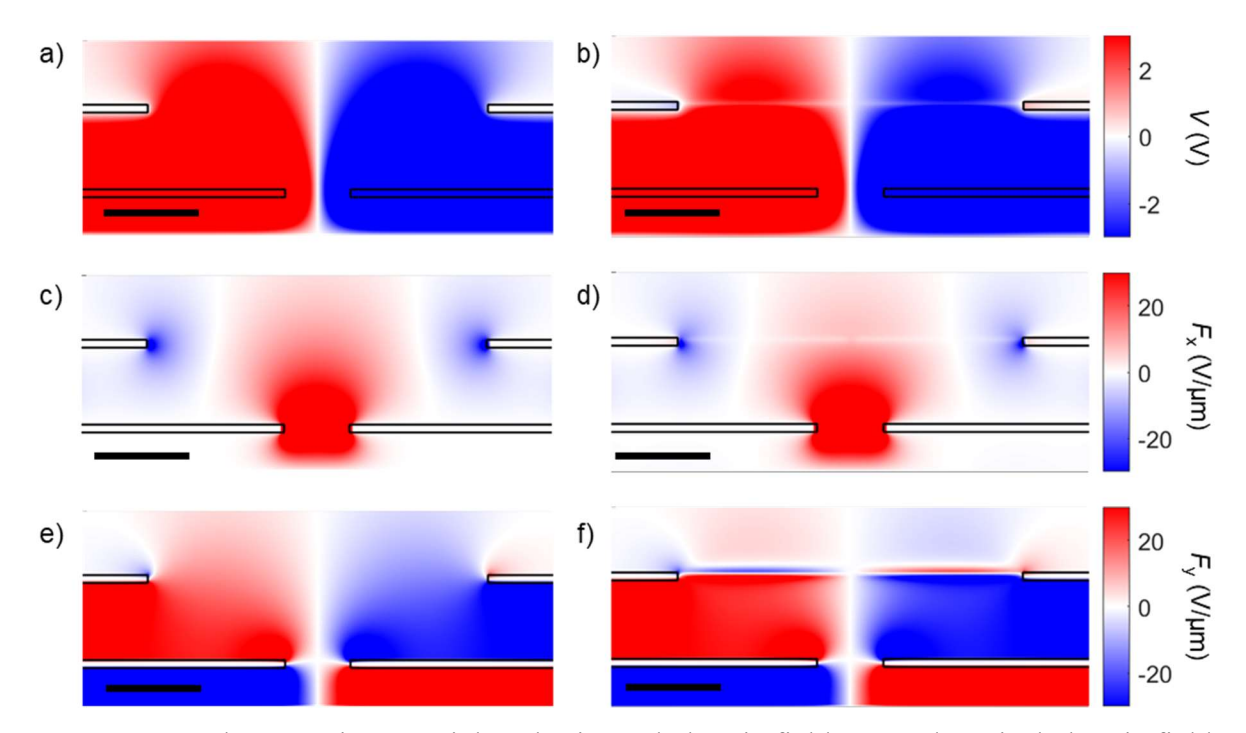


Figure S16. Electrostatic potential, V, horizontal electric field, F_x , and vertical electric field, F_y , when there is no CNT in the device (a, c, e) and when the CNT's charge density is included (b, d, f). All scale bars are 0.75 μ m. The black outlines indicate the location of the contacts and gates. The CNT bridges the trench at the top of the source and drain electrodes.

A linear charge density on the CNT, $\lambda(x)$, is then calculated using an iterative self-consistent process (see Section 3 of the SI). The final electrostatic potential satisfies the following condition: the potential along the left side of the CNT is equal to V_S , and the potential along the right side of the CNT is equal V_D . The self-consistent charge density is shown in Figure S17a. The vertical component of the self-consistent electric field is shown in Figure S17b.

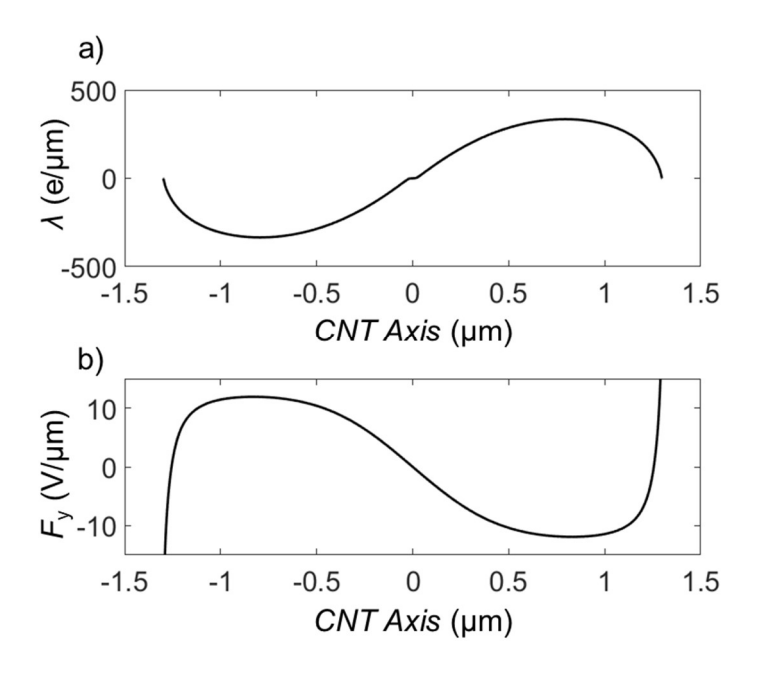


Figure S17. a) Charge density along the CNT axis. The discontinuity at the center corresponds to the intrinsic region in the center of the semiconducting CNT. b) The vertical component of the electric field along the CNT axis, $F_y(x)$.

The CNT experiences a force pulling it towards the gates. The force per unit length (in the vertical direction) is equal to the product of $F_y(x)$ and $\lambda(x)$. This force causes the CNT to bend and stretch. The height of CNT changes from $\Delta y(x) = 0$ to $\Delta y(x) < 0$. Our goal is to calculate the new equilibrium position of the CNT.

To find the equilibrium position of the CNT, we applied the elastic catenary model.¹¹ For this purpose, we replace the CNT with a spring that can stretch in response to the tension due to the horizontal and normal electrostatic forces.

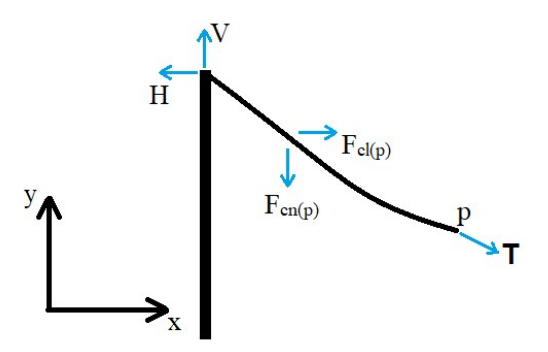


Figure S18. Forces acting on the CNT.

Figure S18 shows a segment of CNT hanging from the supporting electrode and all forces that are exerted on this segment. These forces must be in balance in equilibrium. The non-stretched length of the CNT is L_0 that is placed at a height t from the gates. We consider the position of the non-stretched CNT to be s and the stretched CNT to be p. Then we get,

$$T\frac{dx}{dp} = H - F_{cl}(p)$$

$$T\frac{dy}{dp} = V - F_{cn}(p)$$

where T is the tension, H is the horizontal component of the tension, V is the vertical reaction of the supporting electrode, and F_{cl} and F_{cn} are the horizontal and normal electrostatic forces. Applying Hook's law, we obtain,

$$T = YA \left(\frac{dp}{ds} - 1\right)$$

Where Y is Young's modulus of graphite Y = 1060 GPa¹² and $A = \pi D h$ is the cross-sectional area, where h = 3.4 Å is the graphene thickness. For Device 1, we find YA = 2.28 µN. Based on Figure S18, the following geometrical constraint must be satisfied,

$$\left(\frac{dx}{dp}\right)^2 + \left(\frac{dy}{dp}\right)^2 = 1$$

Therefore, we can write the tension as,

$$T = \sqrt{\left(H - F_{cl}(p)\right)^2 + \left(V - F_{cn}(p)\right)^2}$$

Now, the position of CNT is found,

$$x(s) = \int_0^s (H - F_{cl}(s')) \left[\frac{1}{YA} + \frac{1}{\sqrt{(H - F_{cl}(s'))^2 + (V - F_{cn}(s'))^2}} \right] ds'$$

$$y(s) = t + \int_0^s (V - F_{cn}(s')) \left[\frac{1}{YA} + \frac{1}{\sqrt{(H - F_{cl}(s'))^2 + (V - F_{cn}(s'))^2}} \right] ds'$$

Where $V = 0.5F_{cl}(L_0)$ and H must be found applying the following boundary conditions,

B. C.
$$\begin{cases} x = 0, \ y = t, \ s = 0 \\ x = L_0, \ y = t, \ s = L_0 \end{cases}$$

Figure S19a shows the predicted profile of a suspended CNT under various split gate voltages $(V_{G1} = -V_{G2})$. The magnitude of F_{cn} has local maxima near the peaks of $|\lambda(x)|$, giving the profile a trapezoidal-like shape. In the oil environment, the capacitance between the CNT and the gates is larger than in vacuum. This increases the net force on the CNT. Figure S19b shows the predicted height of the CNT midpoint in the vacuum environment (blue) and oil environment (black).

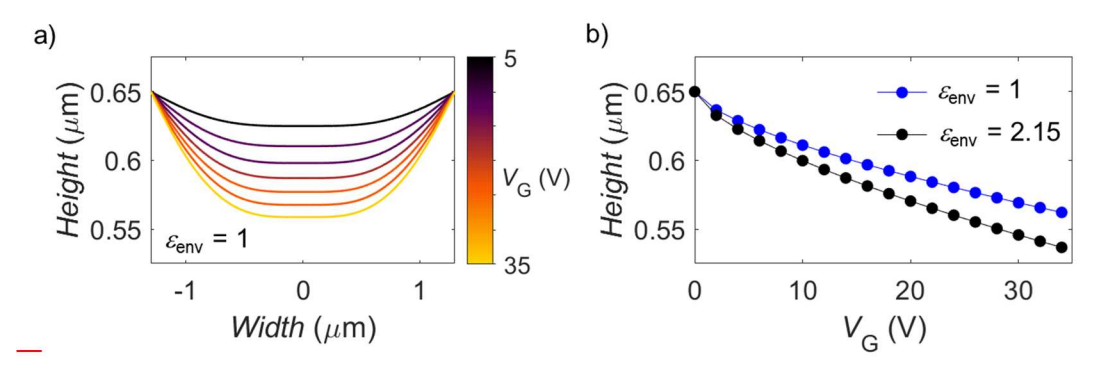


Figure S19. a) The predicted height profile of a suspended CNT in vacuum at various split-gate voltages (± 5 V, ± 10 V, ± 15 V, ± 20 V, ± 25 V, ± 30 V, ± 35 V). The CNT diameter is 2 nm. b) The predicted height of the CNT mid-point a vacuum environment (blue) and oil environment (black).

The electromechancial model described above is most accurate for small displacements of the CNT. We assumed no vertical displacement of the CNT when we calculated the charge density, $\lambda(x)$. For a more refined model, the CNT height profile should be feed back into the calculation of $\lambda(x)$ to find a self-consistent solution (an iterative process). The full self-consistent solution

would deviate from our simple model at large gate voltages. The goal of our simple model is to demonstrate that mechanical strain is a reasonable explanation for the shift in exciton resonance. Indeed, the simple model agrees very well with experiment when $V_G < 10 \text{ V}$ (Fig. 3c and 3d in the main text).

12. Photocurrent Peak Fitting

In the main text, we calculate the photocurrent quantum yield, η , as

$$\eta = \frac{\int I_{\rm PC} d(\hbar\omega)}{e\Phi L N_{\rm L} \int \alpha d(\hbar\omega)}.$$

To find the numerator, $\int I_{PC} d(\hbar\omega)$, the photocurrent peaks are fit with a Lorentzian function, G, given by

$$G = \frac{s}{(\hbar\omega - t)^2 + u^2} + G_0,$$

where G_0 is the vertical offset, u is the half-width at half-maximum of the peak, t is the peak center, and $s/u^2 = \max(G - G_0)$. We take $\int I_{PC} d(\hbar\omega) = \int (G - G_0) d(\hbar\omega) = \pi s/u$. Lorentzian fits for all photocurrent spectra are plotted in the next section.

13. Comparing Photocurrent Quantum Yield to an Alternative Model

Before developing a detailed model to explain the field dependence of photocurrent quantum yield, we compared our measurements to a simple model that ignores the effect of exciton binding energy and impact ionization. As shown below, this simple model fails to describe the shape of the measured $\eta(F)$ function.

The escape time $\tau_{\rm esc}$ for a free carrier in the intrinsic region of the CNT diode can be estimated as

$$\tau_{\rm esc} = L/v$$
,

where $L = (E_G/e - V_{SD})/F$ is the length of the intrinsic region, and v is the velocity of the free carrier. The velocity, v, depends on the axial electric field, F. The velocity saturation model predicts¹³

$$v = \left(\frac{1}{\mu F} + \frac{1}{v_{\text{sat}}}\right)^{-1},$$

where $\mu \approx 10^4$ cm²/V·s is the carrier mobility in the undoped CNT,¹⁴ and $v_{\rm sat} \approx 5 \times 10^7$ cm/s is the saturation velocity.¹³ The predicted velocity is shown in Fig S20a. For the fields used in our experiment (F > 3 V/ μ m), the velocity reaches the saturation value.

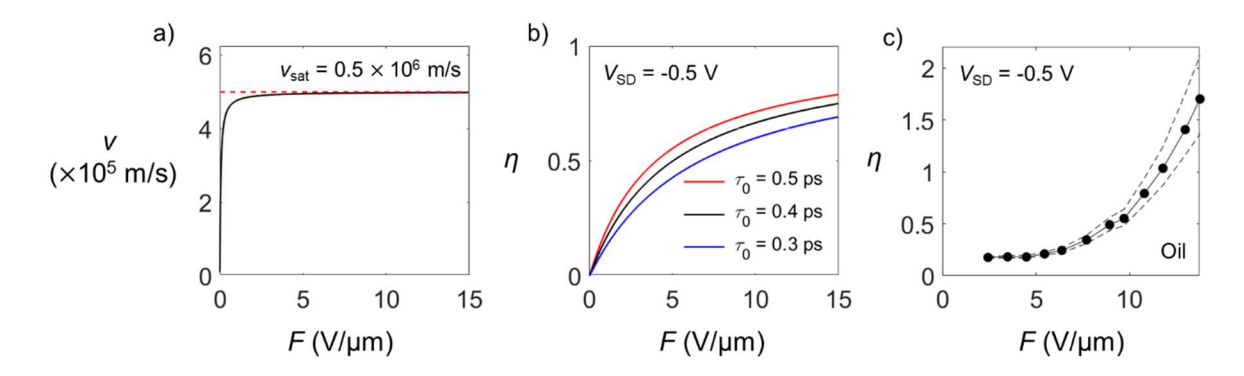


Figure S20. a) Charge carrier velocity, v, is fully saturated when F > 3 V/μm. b) Predicted photocurrent quantum yield using the "escape-before-recombination" model (see text) with $\tau_0 = 0.5$ ps (red), 0.4 ps (black), and 0.3 ps (blue), and $E_G/e - V_{SD} = 1$ V. c) Experimentally determined photocurrent quantum yield for Device 1, illuminated with $\hbar\omega = S_{22}$, in the oil environment (the same data is shown in Fig. 4 of the main text).

To predict η from this model, we calculated the fraction of carriers that would escape before recombining, assuming a constant recombination rate $1/\tau_0$,

$$\eta = \frac{1/\tau_{\rm esc}}{1/\tau_0 + 1/\tau_{\rm esc}}.$$

In Fig. S20b, we plot this function using various values of τ_0 . There is no value of τ_0 that reproduces the shape of the measured $\eta_{22}(F)$ curve (Fig. S20c).

14. Supplemental Photocurrent Data and Quantum Yield at S₃₃ for Devices 2 and 3.

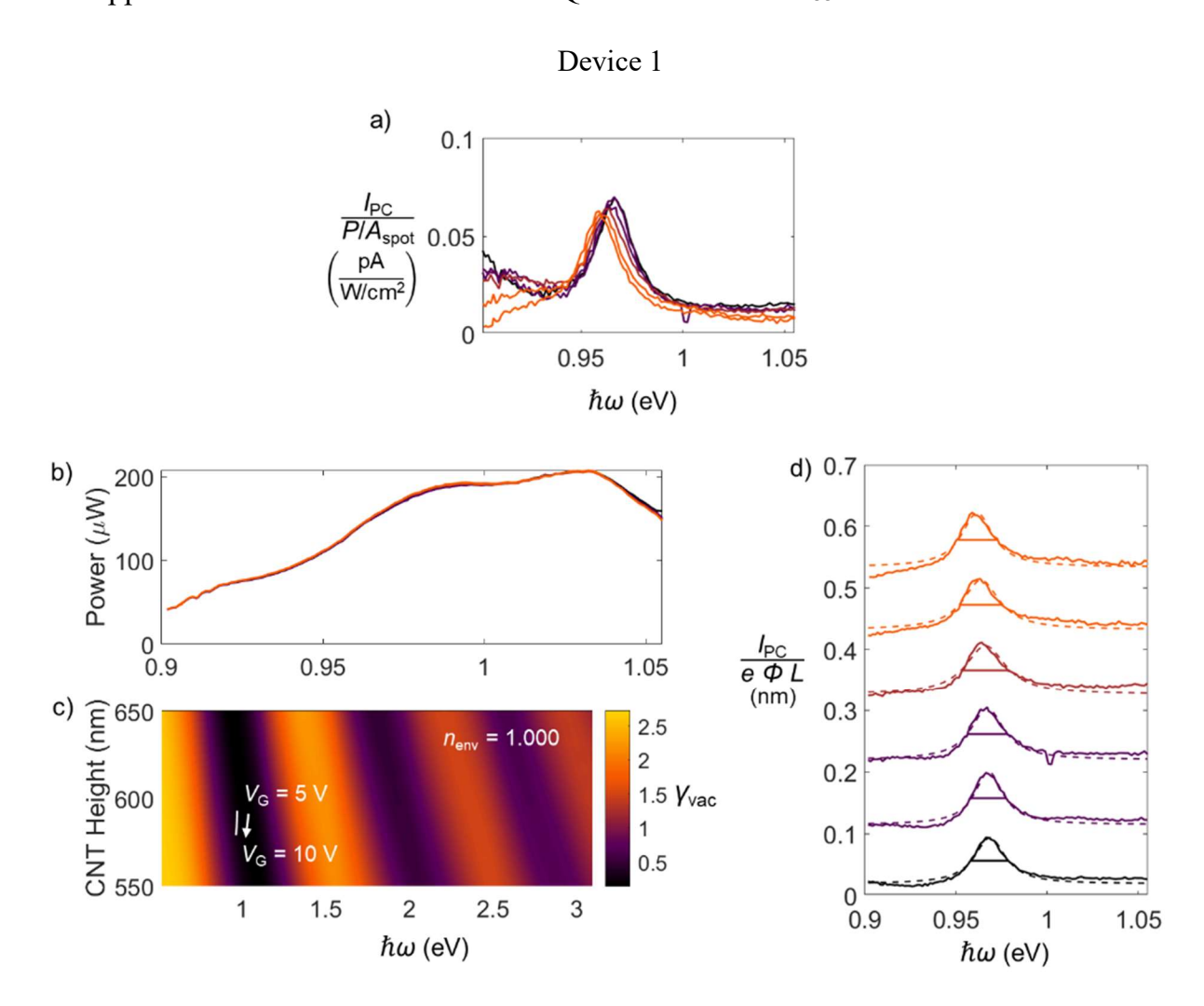


Figure S21. a) Photocurrent spectra normalized for laser intensity in the vicinity of S_{22} in air as V_G is increase from 5 to 10 V with $V_{SD} = -0.5$ V. b) Laser power used to normalize photocurrent spectra. c) FDTD simulated γ in vacuum against photon energy and the height of the CNT's intrinsic region above the gates. White line: The CNT's height against the energy of the S_{22} resonance. The CNT's intrinsic region moves to increased γ as gate voltage is increased. d) Photocurrent spectra of the S_{22} resonance normalized for the photon flux and the intrinsic region length in vacuum. Spectra are offset for clarity. V_G is increased from 5 to 10 V (from black curve to orange curve). Each spectrum is fit with a Lorentzian (dashed lines) that is integrated to determine the oscillator strength. The horizontal lines display the FWHM of the Lorentzian fit.

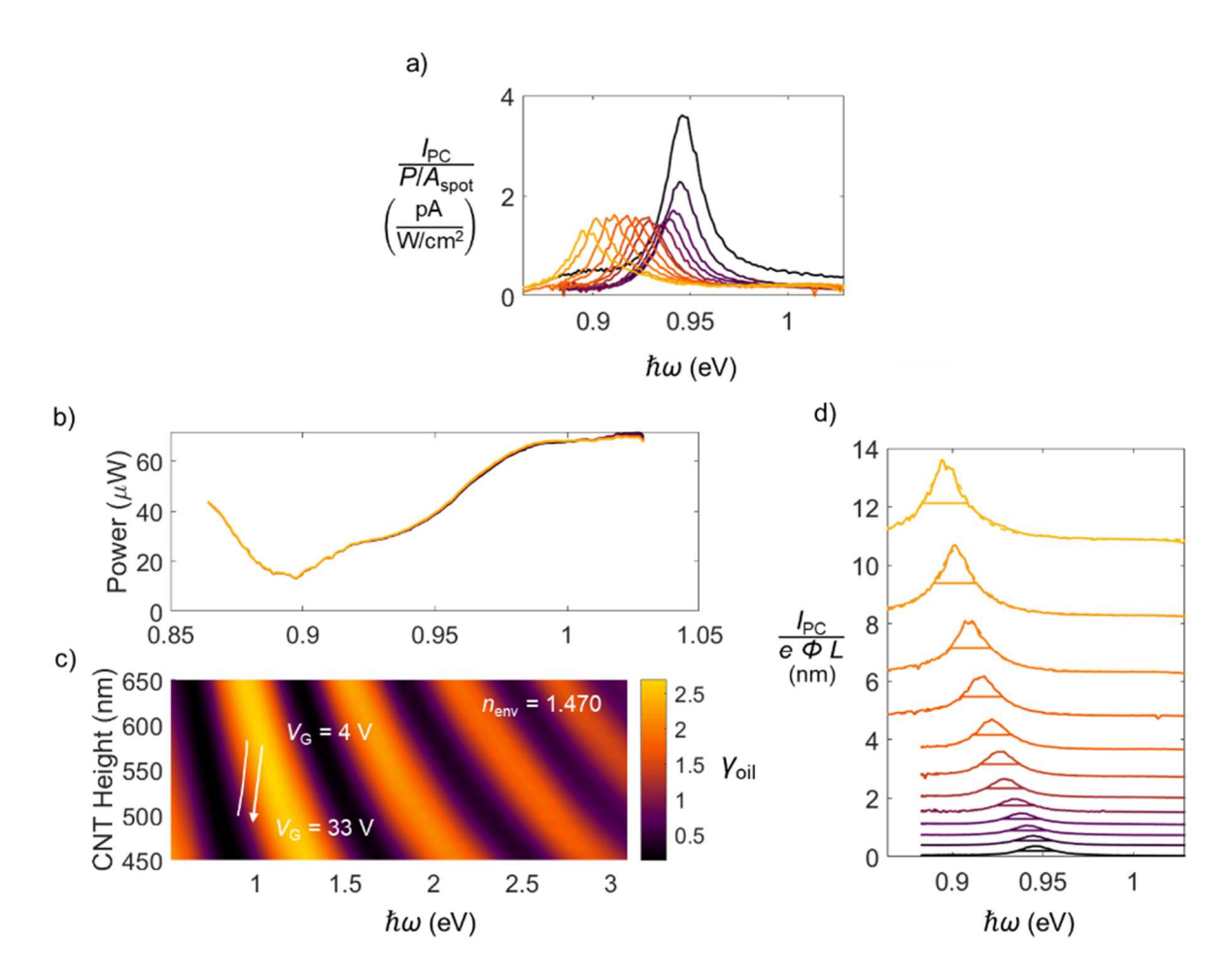


Figure S22. a) Photocurrent spectra normalized for laser intensity in the vicinity of S_{22} in dielectric oil as V_G is increase from 4 to 33 V with $V_{SD} = -0.5$ V. b) Laser power used to normalize photocurrent spectra. c) FDTD simulated γ in oil against photon energy and the height of the CNT's intrinsic region above the gates. White line: The CNT's height against the energy of the S_{22} resonance. The CNT's intrinsic region moves to decreased γ as gate voltage is increased. d) Photocurrent spectra of the S_{22} resonance normalized for the photon flux and the intrinsic region length in oil. Spectra are offset for clarity. V_G is increased from 4 to 33 V (from black curve to orange curve). Each spectrum is fit with a Lorentzian (dashed lines) that is integrated to determine the oscillator strength. The horizontal lines display the FWHM of the Lorentzian fit.

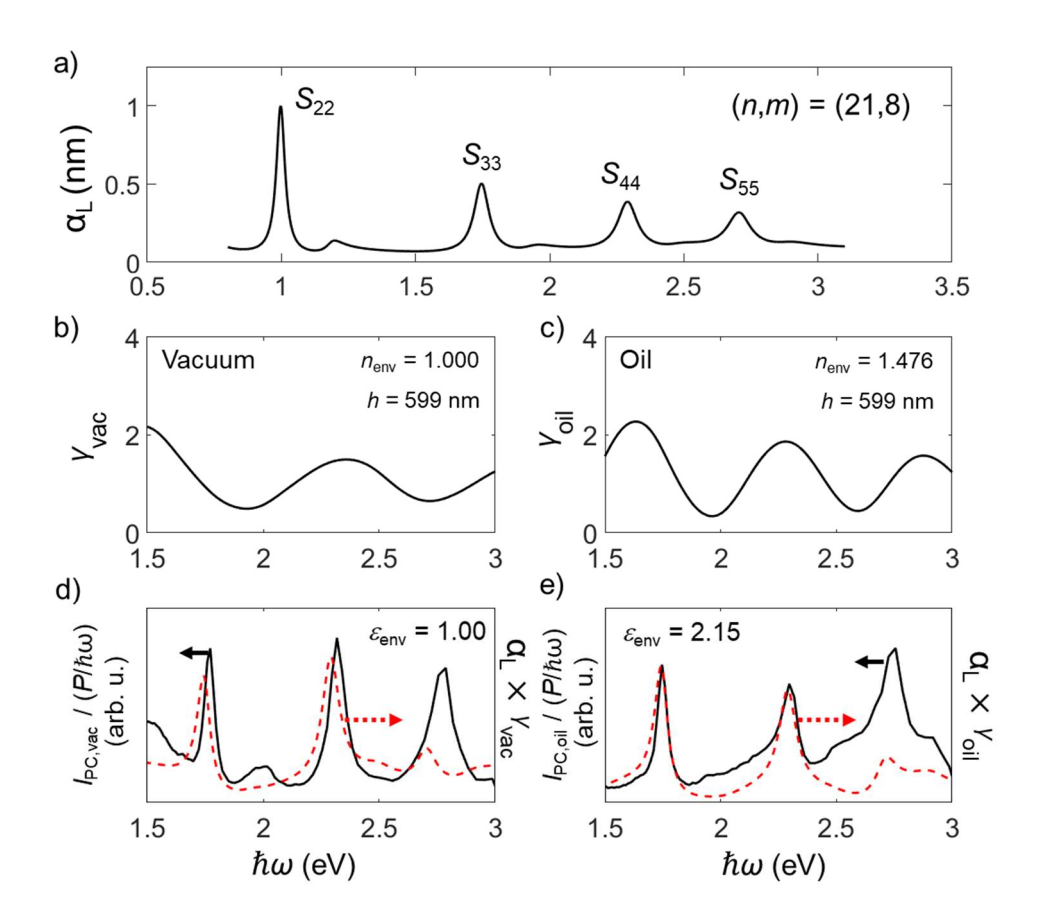


Figure S23. Finding the CNT chirality and as-grown height for Device 2. a) The empirical absorption cross section per length of a CNT with chirality (21,08). b) γ calculated in FDTD simulations for the vacuum environment using $h_0 = 599$ nm. c) γ calculated in FDTD simulations for the oil environment using $h_0 = 599$ nm. d) Photocurrent spectrum measured in the vacuum environment normalized for $P/\hbar\omega$ (black) plotted along with $\gamma_{\rm ac}\alpha_{\rm L}$ (red dashes). e) Photocurrent spectrum measured in the oil environment normalized for $P/\hbar\omega$ (black) plotted along with $\gamma_{\rm oil}\alpha_{\rm L}$ (red dashes).

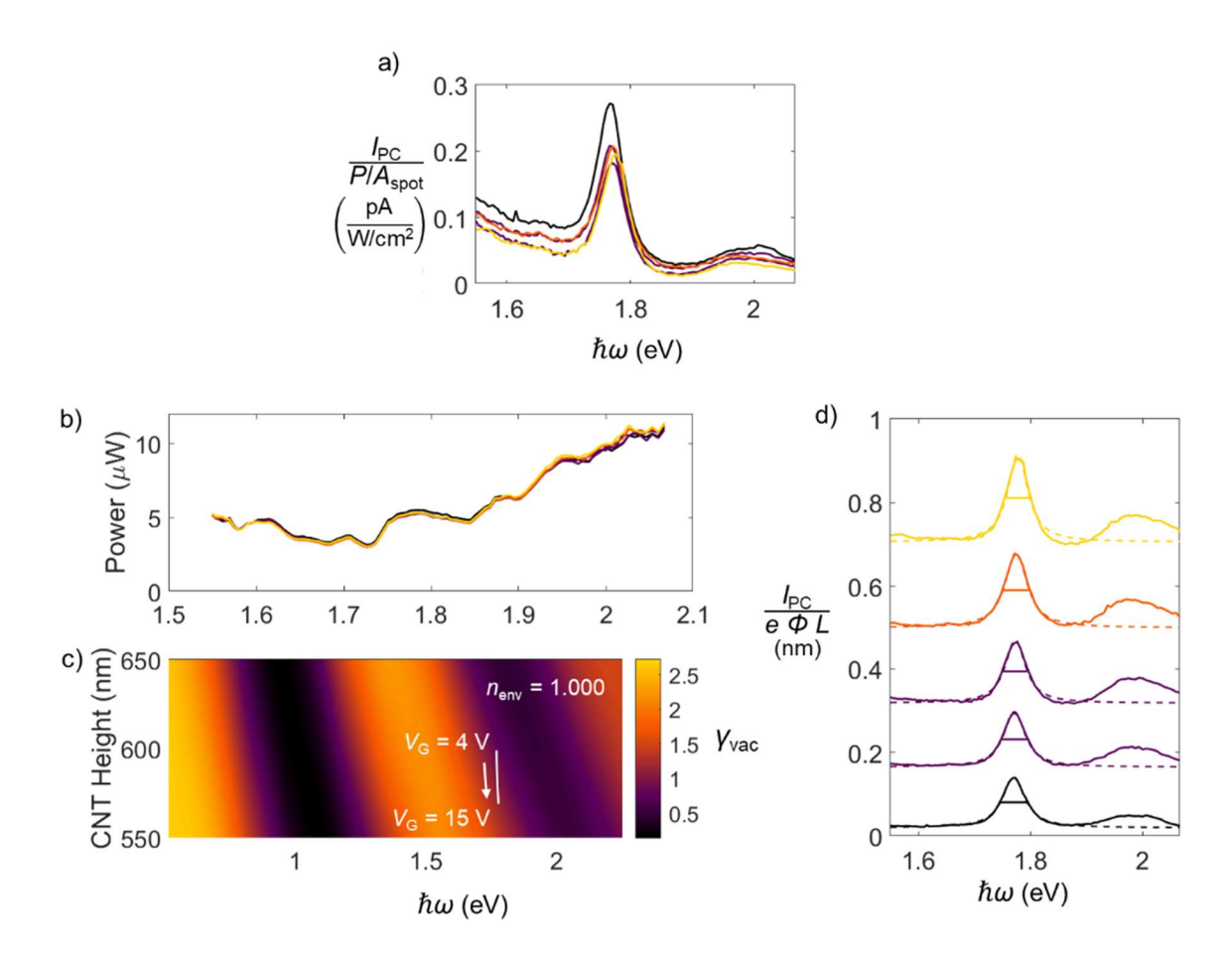


Figure S24. a) Photocurrent spectra normalized for laser intensity in the vicinity of S_{33} in vacuum as V_G is increase from 4 to 15 V with $V_{SD} = -0.5$ V. b) Laser power used to normalize photocurrent spectra. c) FDTD simulated γ in vacuum against photon energy and the height of the CNT's intrinsic region above the gates. White line: The CNT's height against the energy of the S_{33} resonance. The CNT's intrinsic region moves to increased γ as gate voltage is increased. d) Photocurrent spectra of the S_{33} resonance normalized for the photon flux and the intrinsic region length in vacuum. Spectra are offset for clarity. V_G is increased from 4 to 15 V (from black curve to orange curve). Each spectrum is fit with a Lorentzian (dashed lines) that is integrated to determine the oscillator strength. The horizontal lines display the FWHM of the Lorentzian fit.

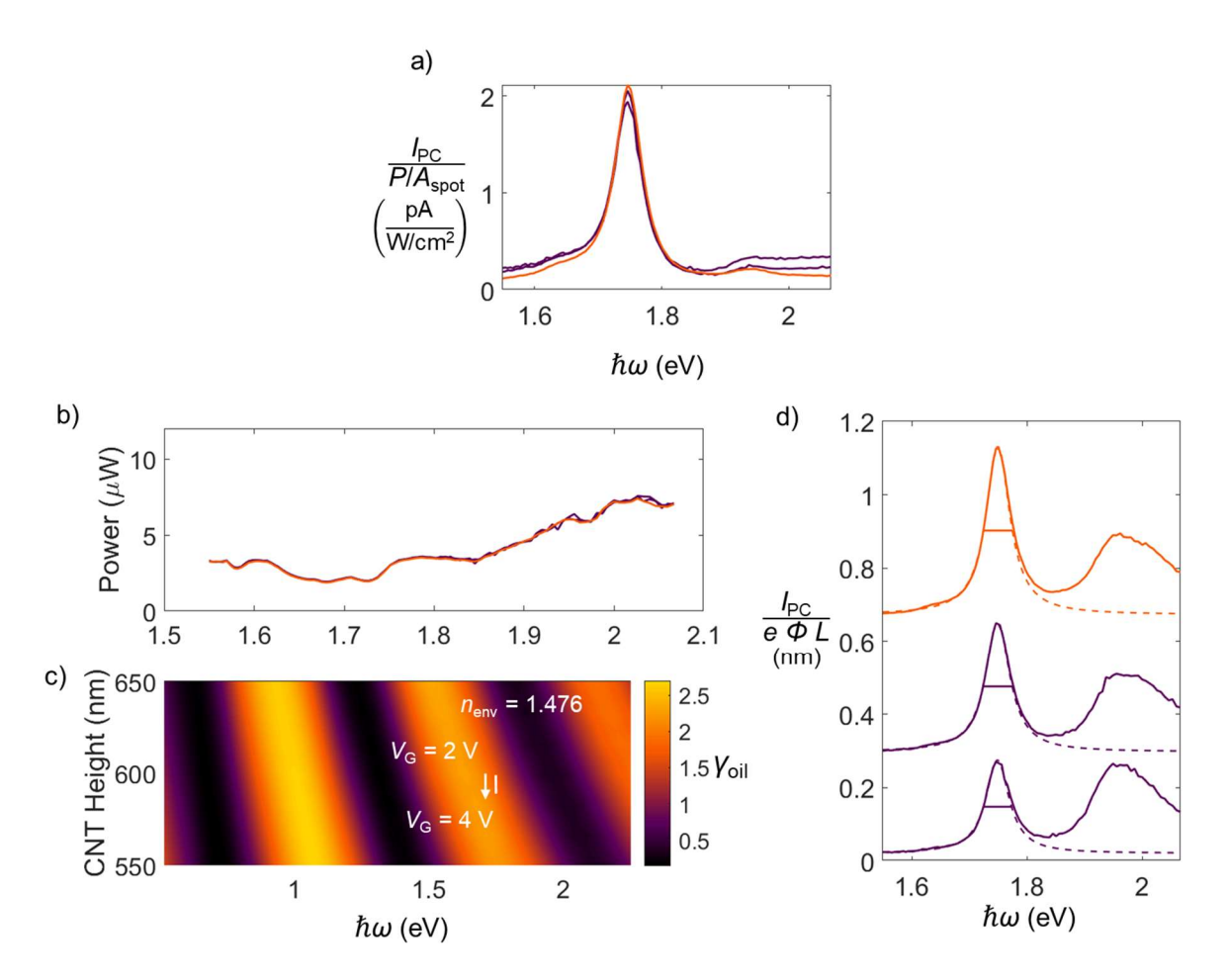


Figure S25. a) Photocurrent spectra normalized for laser intensity in the vicinity of S_{33} in dielectric oil as V_G is increase from 2 to 4 V with $V_{SD} = -0.5$ V. b) Laser power used to normalize photocurrent spectra. c) FDTD simulated γ in oil against photon energy and the height of the CNT's intrinsic region above the gates. White line: The CNT's height against the energy of the S_{33} resonance. The CNT's intrinsic region moves to increased γ as gate voltage is increased. d) Photocurrent spectra of the S_{33} resonance normalized for the photon flux and the intrinsic region length in oil. Spectra are offset for clarity. V_G is increased from 2 to 4 V (from black curve to orange curve). Each spectrum is fit with a Lorentzian (dashed lines) that is integrated to determine the oscillator strength. The horizontal lines display the FWHM of the Lorentzian fit.

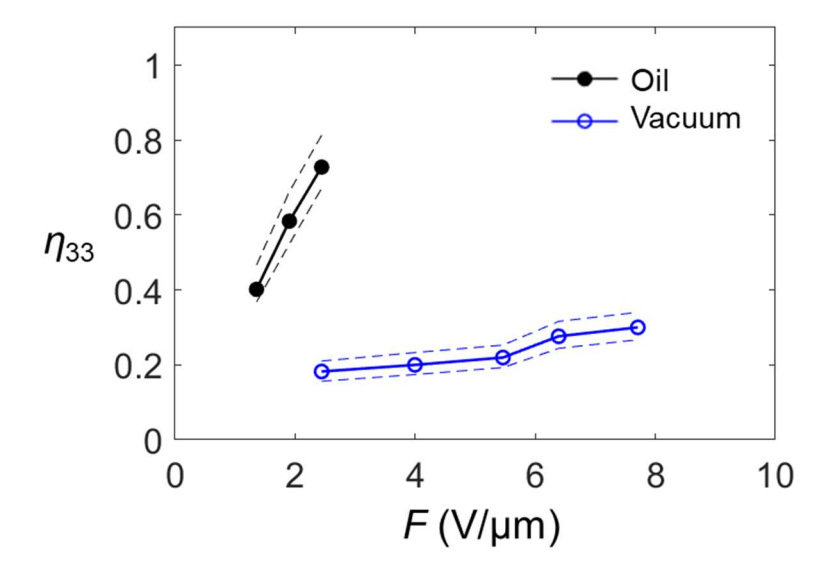


Figure S26. Calculated photocurrent quantum yield against field in oil and in vacuum for S_{33} of Device 2. Dashed lines are η_{33} calculated with the CNT's resting height increased or decreased by 10 nm.

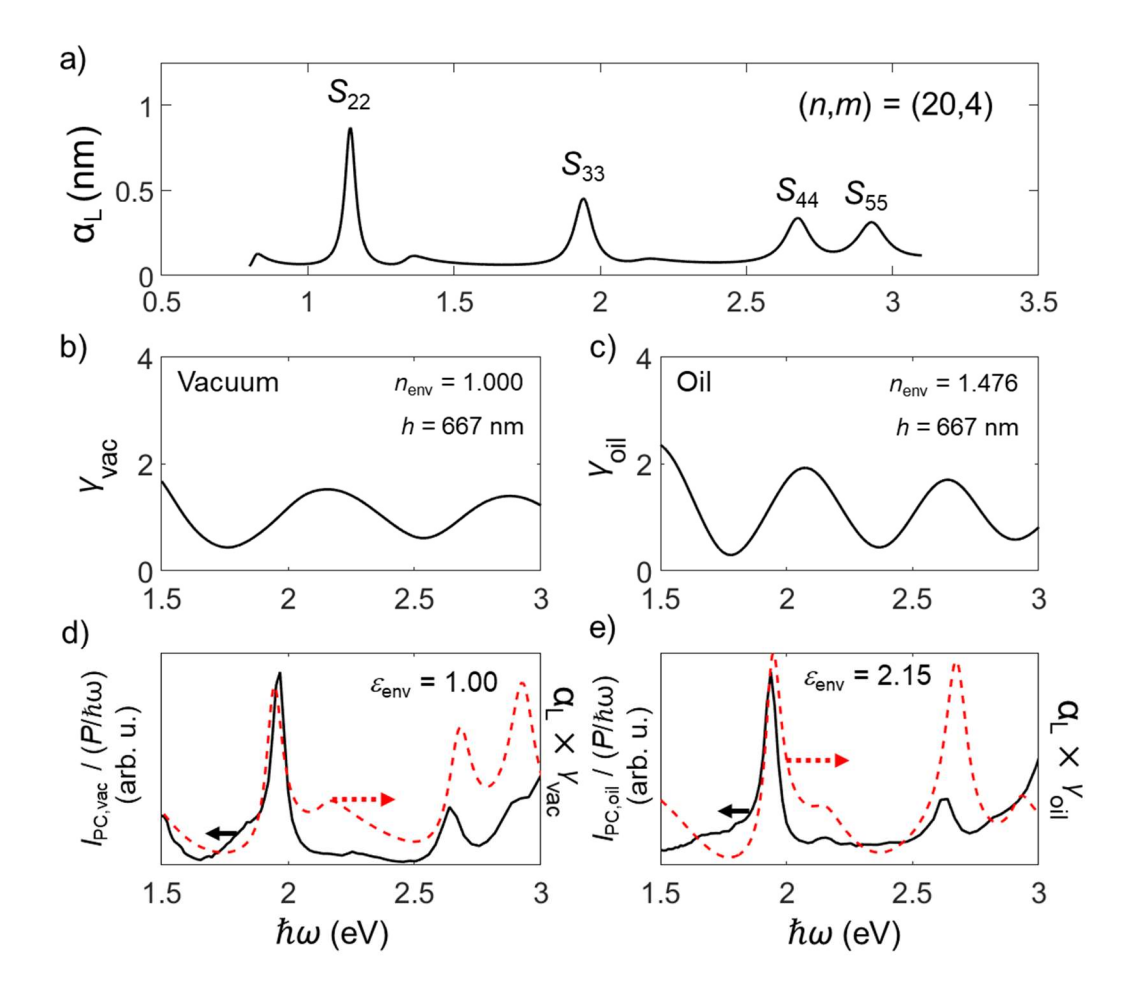


Figure S27. Finding the CNT chirality and as-grown height for Device 2. a) The empirical absorption cross section per length of a CNT with chirality (20,04). b) γ calculated in FDTD simulations for the vacuum environment using $h_0 = 667$ nm. c) γ calculated in FDTD simulations for the oil environment using $h_0 = 667$ nm. d) Photocurrent spectrum measured in the vacuum environment normalized for $P/\hbar\omega$ (black) plotted along with $\gamma_{\rm ac}\alpha_{\rm L}$ (red dashes). e) Photocurrent spectrum measured in the oil environment normalized for $P/\hbar\omega$ (black) plotted along with $\gamma_{\rm oil}\alpha_{\rm L}$ (red dashes).

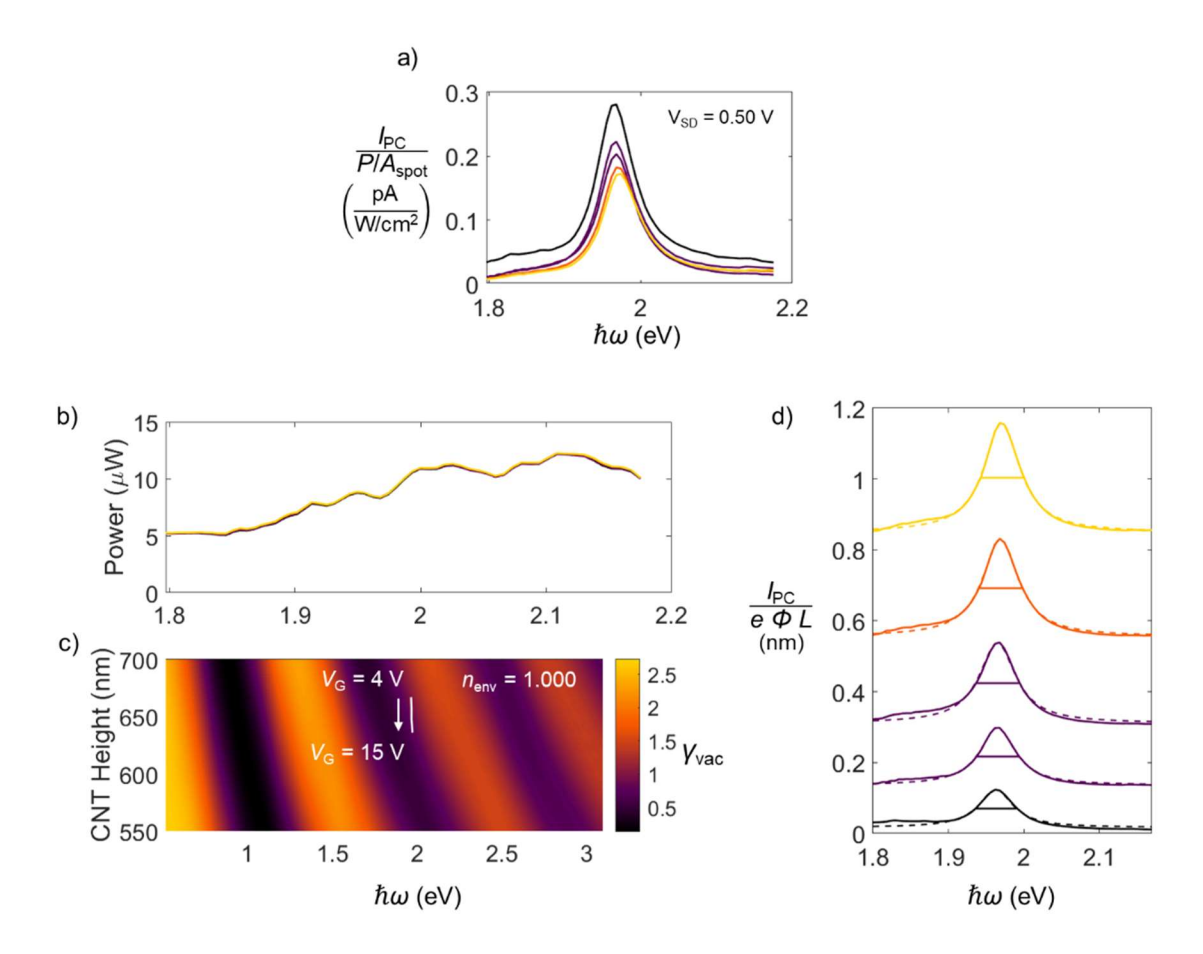


Figure S28. a) Photocurrent spectra normalized for laser intensity in the vicinity of S_{33} in vacuum as V_G is increase from 4 to 15 V with $V_{SD} = -0.5$ V. b) Laser power used to normalize photocurrent spectra. c) FDTD simulated γ in vacuum against photon energy and the height of the CNT's intrinsic region above the gates. White line: The CNT's height against the energy of the S_{33} resonance. The CNT's intrinsic region moves to increased γ as gate voltage is increased. d) Photocurrent spectra of the S_{33} resonance normalized for the photon flux and the intrinsic region length in vacuum. Spectra are offset for clarity. V_G is increased from 4 to 15 V (from black curve to orange curve). Each spectrum is fit with a Lorentzian (dashed lines) that is integrated to determine the oscillator strength. The horizontal lines display the FWHM of the Lorentzian fit.

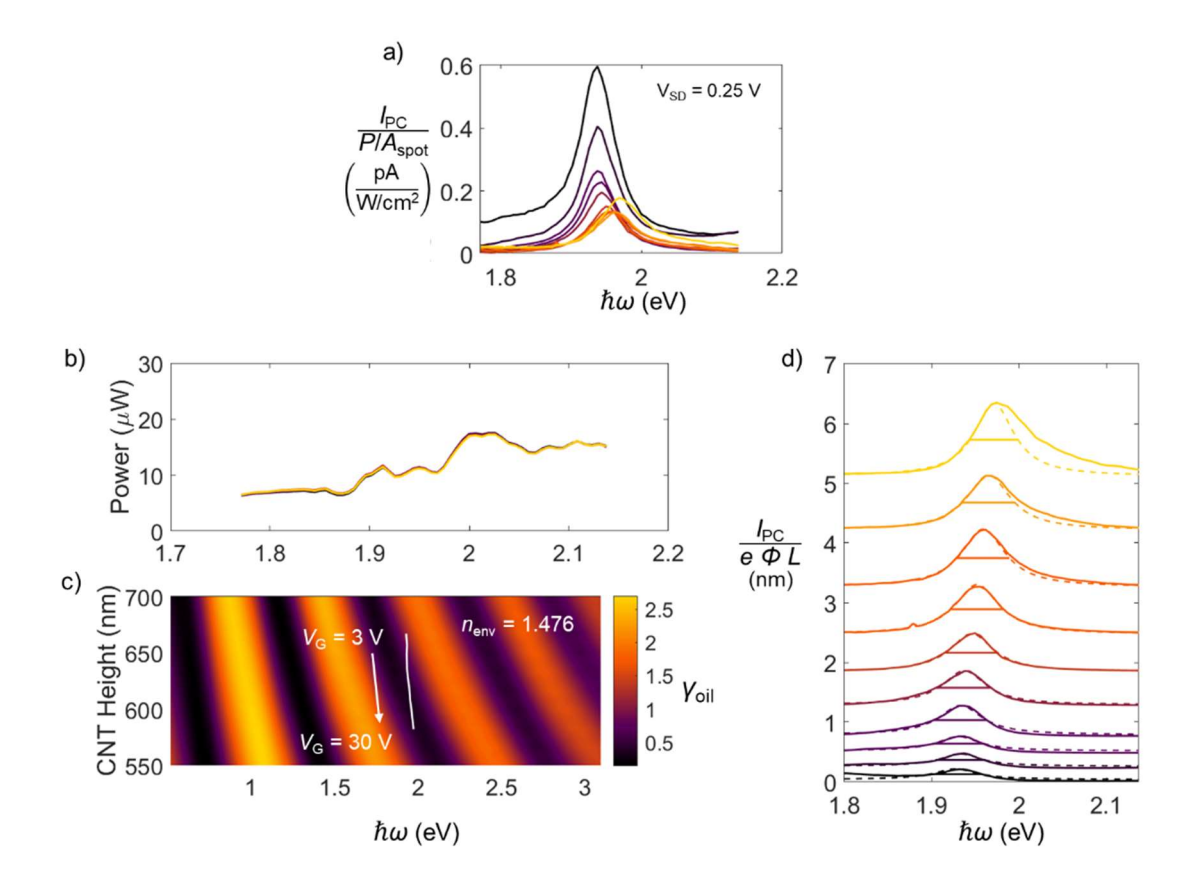


Figure S29. a) Photocurrent spectra normalized for laser intensity in the vicinity of S_{33} in dielectric oil as V_G is increase from 3 to 30 V with $V_{SD} = -0.25$ V. b) Laser power used to normalize photocurrent spectra. c) FDTD simulated γ in oil against photon energy and the height of the CNT's intrinsic region above the gates. White line: The CNT's height against the energy of the S_{33} resonance. The CNT's intrinsic region moves to increased γ as gate voltage is increased. d) Photocurrent spectra of the S_{33} resonance normalized for the photon flux and the intrinsic region length in oil. Spectra are offset for clarity. V_G is increased from 3 to 30 V (from black curve to orange curve). Each spectrum is fit with a Lorentzian (dashed lines) that is integrated to determine the oscillator strength. The horizontal lines display the FWHM of the Lorentzian fit.

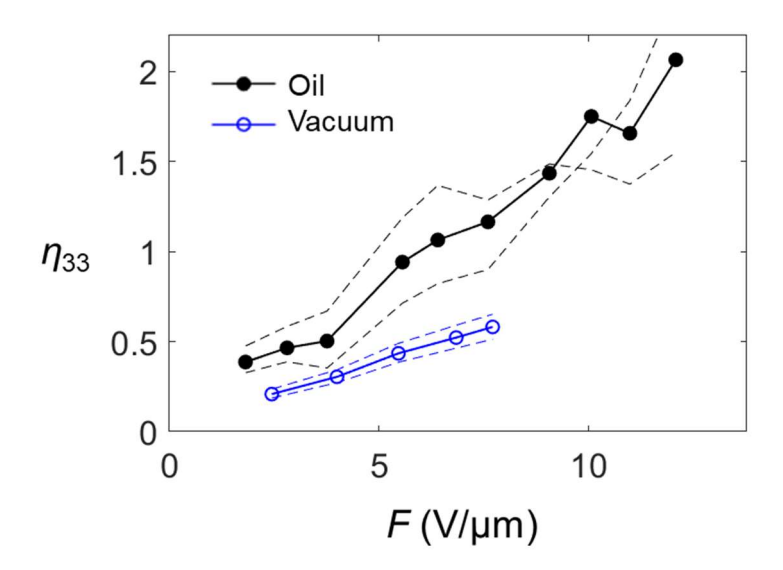


Figure S30. Calculated photocurrent quantum yield against field in oil and in vacuum for S_{33} of Device 3. Dashed lines are η_{33} calculated with the CNT's resting height increased or decreased by 10 nm.

References for the SI -

- (1) Aspitarte, L.; McCulley, D. R.; Minot, E. D. A Nanoscale *pn* Junction in Series with Tunable Schottky Barriers. *J. Appl. Phys.* **2017**, *122*, 134304.
- (2) Khodier, S. A. Refractive Index of Standard Oils as a Function of Wavelength and Temperature. *Opt. Laser Technol.* **2002**, *34*, 125–128.
- (3) McCulley, D. R.; Senger, M. J.; Bertoni, A.; Perebeinos, V.; Minot, E. D. Extremely Efficient Photocurrent Generation in Carbon Nanotube Photodiodes Enabled by a Strong Axial Electric Field. *Nano Lett.* **2020**, *20*, 433–440.
- (4) Lumerical Inc. FDTD. https://www.lumerical.com/products/fdtd (accessed December 11, 2019).
- (5) Palik, E. D. Handbook of Optical Constants of Solids, I.; Academic Press: Orlando, 1997.
- (6) Liu, K.; Deslippe, J.; Xiao, F.; Capaz, R. B.; Hong, X.; Aloni, S.; Zettl, A.; Wang, W.; Bai, X.; Louie, S. G.; Wang, E.; Wang, F. An Atlas of Carbon Nanotube Optical Transitions. *Nat. Nanotechnol.* 2012, 7, 325–329.
- (7) Liu, K.; Hong, X.; Choi, S.; Jin, C.; Capaz, R. B.; Kim, J.; Wang, W.; Bai, X.; Louie, S. G.; Wang, E.; Wang, F. Systematic Determination of Absolute Absorption Cross-Section of Individual Carbon Nanotubes. *Proc. Natl. Acad. Sci.* 2014, 111, 7564–7569.
- (8) Suk, J. W.; Kitt, A.; Magnuson, C. W.; Hao, Y.; Ahmed, S.; An, J.; Swan, A. K.; Goldberg, B. B.; Ruoff, R. S. Transfer of CVD-Grown Monolayer Graphene onto Arbitrary Substrates. *ACS Nano* **2011**, *5*, 6916–6924.
- (9) Huang, M.; Wu, Y.; Chandra, B.; Yan, H.; Shan, Y.; Heinz, T. F.; Hone, J. Direct Measurement of Strain-Induced Changes in the Band Structure of Carbon Nanotubes. *Phys. Rev. Lett.* **2008**, *100*, 1–4.
- (10) Perebeinos, V.; Avouris, P. Exciton Ionization, Franz-Keldysh, and Stark Effects in Carbon Nanotubes. *Nano Lett.* **2007**, *7*, 609–613.
- (11) Irvine, H. M. *Cable Structures*; MIT Press Series in Structural Mechanics; MIT Press: Cambridge, Mass., 1981.
- (12) Blakslee, O. L.; Proctor, D. G.; Seldin, E. J.; Spence, G. B.; Weng, T. Elastic Constants of Compression-Annealed Pyrolytic Graphite. *J. Appl. Phys.* **1970**, *41*, 3373–3382.
- (13) Perebeinos, V.; Tersoff, J.; Avouris, P. Electron-Phonon Interaction and Transport in Semiconducting Carbon Nanotubes. *Phys. Rev. Lett.* **2005**, *94*, 2–5.

(14) Gabor, N. M.; Zhong, Z.; Bosnick, K.; McEuen, P. L. Ultrafast Photocurrent Measurement of the Escape Time of Electrons and Holes from Carbon Nanotube *p-i-n* Photodiodes. *Phys. Rev. Lett.* **2012**, *108*, 1–5.